

Not available on line

Not available on line

**Task Title: STRESS CORROSION CRACKING BEHAVIOUR OF EUROFER'97
IN WATER WITH ADDITIVES**

INTRODUCTION

In the framework of a previous task (SM3.3) concerning the Structural Materials, a study was carried out to assess:

- the general corrosion behaviour,
- the pitting susceptibility and,
- the Stress Corrosion Cracking (SCC) susceptibility.

of Low Activation (LA) steels. These materials are EUROFER'97 and F82H.

In the framework of the task TW1-TTMS-003-D12, complementary tests were performed to assess the SCC behaviour of EUROFER'97 in high temperature water.

2003 ACTIVITIES

The material studied in the framework of this study is EUROFER'97 (heat E83698). This material was supplied by BÖHLER as plates of 1.5 mm thick.

Its chemical composition is given in table 1.

*Table 1 : Chemical composition of EUROFER'97
(in wt %)*

C	0.11
Cr	8.96
Mn	0.49
Si	0.04
W	1.08
V	0.20
Ni	0.02
Ta	0.14
N	0.021
P	< 0.005
S	0.004
Fe	Bal.

The material is tested in the "as received" condition: normalized 980°C/0.5 hour then tempered 760°C/1.5 hour.

The microstructure is martensitic without delta ferrite. The grain size of the high temperature austenitic phase is between 10 and 15 µm. The Vickers microhardness of the bulk metal is about 230 HV(4.905N).

The tensile properties of this material at 320°C are:

1. 0.2 % yield stress: 550 MPa,
2. Ultimate tensile stress: 675 MPa,
3. Total elongation: 25 %.

The corrosion test medium was prepared by adding to deionized water (resistivity 18 MΩ.cm) lithium as lithia (LiOH) in order to obtain a pH of 7 at the test temperature: 320°C. 2.40 10⁻⁵ mol of Li was added to 1 kg of deionized water ([Li] = 166 ppb).

An hydrogen overpressure, controlled with a Pd/Ag probe, was applied to maintain a hydrogen concentration in the liquid medium of about 35 mL (SPT).kg⁻¹ at the test temperature (320°C).

The autoclave is made of AISI 316L Stainless Steel (SS) and has a 1.23 litres inner volume. On the bottom of the autoclave, a Pd/Ag membrane is fixed in order to measure the hydrogen pressure in equilibrium with the dissolved hydrogen in the water. The autoclave heating is insured by 3 heating resistances rolled round the external surface of the autoclave. The design temperature and pressure of the autoclave are respectively 400°C and 20 MPa.

This autoclave is coupled with a tensile machine (figure 1) allowing to perform Constant Extension Rate Tests (CERTs). All the tests are performed at the same elongation rate: 5x10⁻⁸ s⁻¹.



Figure 1 : View of the facility device for CERTs

SCC tests were also performed with U-bends specimens (figure 2).

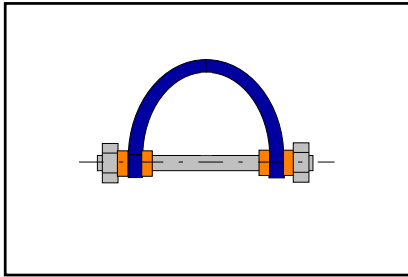


Figure 2 : Schematic representation of a U-Bend specimen

These tests are performed in a corrosion loop. This loop consists of an autoclave linked to a water circuit allowing to insure a continuous water flow and to control the medium chemistry (figure 3). The autoclave is made of AISI 316L SS and has a 5 liters inner volume. At the bottom of the autoclave is fixed a Pd/Ag membrane for measuring the hydrogen pressure in equilibrium with the dissolved hydrogen in the water. The flow rate of the medium was 10 L.h⁻¹ and the working pressure was 15 MPa.



Figure 3 : View of the loop used for the U-Bends

U-Bends were obtained by bending rectangular coupons. The bending of the specimens were performed in two successive steps.

The coupon is plastically strained in order to have an angle of about 45° between the two legs of the specimen. After this first stage, the two legs of the specimens are made parallel with a nut and a screw. The total strain ϵ on the outside of the bend can be closely approximated by the equation (equation 1):

$$\epsilon = \frac{T}{2.R} \quad (\text{equation 1})$$

Where:

T is the thickness of the coupon and
R the radius of the bend curvature.

As the thickness of the coupons is 1 mm and the radius of the bend curvature is about 4 mm, the total deformation on the outside of the bend is roughly equal to 12.5 %.

The stress induced depends on the mechanical properties of the tested materials. By taking into account the curves σ versus ϵ of the material, the stress level at the apex of the U-bends at 320°C are approximately 600 MPa.

It must be noticed that this estimation does not take into account the cold worked layer at the surface of the coupons. As the surface of the material was previously work hardened by the grinding machine, the stress level at the outside of the specimen should be more important than the value given above.

The tensile specimens used for the CERTs were also grinded during the manufacturing. The cold worked layer at the surface of the specimens and the roughness of the surfaces are roughly identical for all of the samples: tensile specimens and coupons used for the U-Bends preparation.

For all of the specimens, the roughnesses are roughly identical: Ra = 0.5 μm .

The outside of the U-bends was examined previously to testing with a Scanning Electron Microscope (SEM). Some surface defects were observed (figure 4).

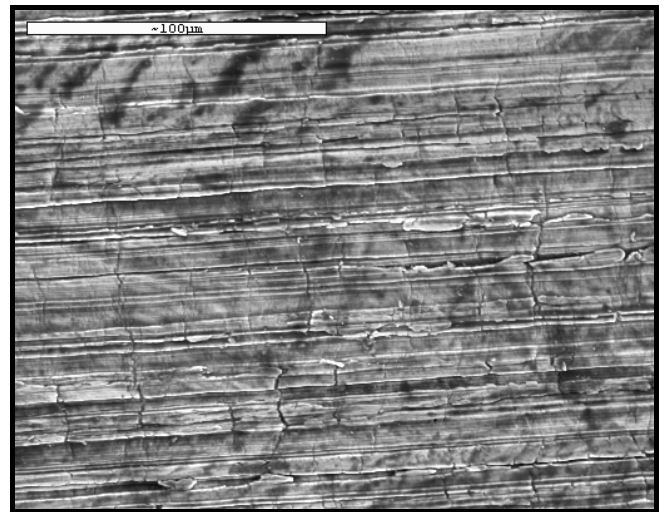


Figure 4 : Outside of a U-Bend specimen before the SCC test

These defects, mainly oriented in the direction of the applied stress, can reach a length of 100 μm , but have a very small depth (< 20 μm). The depths of the surface defects are in accordance with the depth of the cold worked layer induced by grinding.

The reasons why these defects appear in the cold worked layer are both the "low" ductility of the material and mainly the high level of deformation at the surface of the cold worked layer. In this study, the cold worked layer has not been removed in order to have a surface representative of the surface of the components of the future FUSION reactor.

TESTS PERFORMED WITH U-BENDS

The autoclave connected to the loop was opened after 1000 h, 3000 h and 5000 h of test durations.

After each interruption, the U-bends (quantity 3) were observed with a microscope to assess the SCC susceptibility of the material.

After the total test duration of 5000 hours, no macroscopic crack was observed at the surface of the U-Bends (figures 5 and 6).



Figure 5 : View of a U-Bend after 5000 hours of test duration

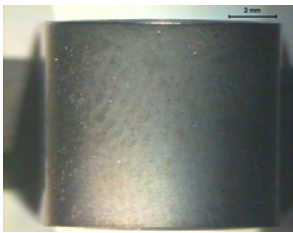


Figure 6 : View of the apex of a U-Bend after 5000 hours of test duration

Microscopic examination of the specimens with SEM shows that the surface defects, observed before the test (figure 7). The depth of these shallow defects is lower than the depth work hardened during the manufacturing.

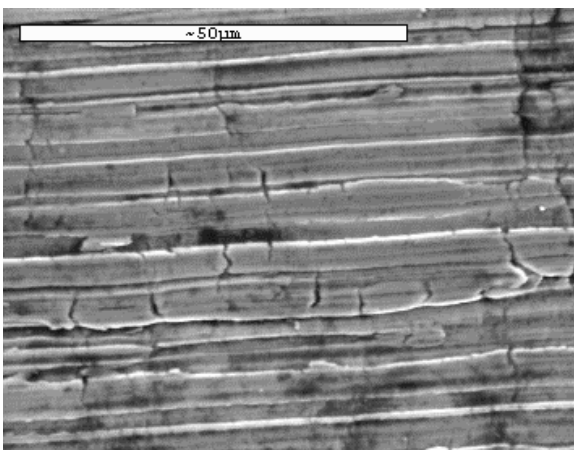


Figure 7 : SEM observation of the apex of a U-Bend after 5000 hours of test duration

CONSTANT EXTENSION RATE TESTS

As for the U-Bends test, the surface of the tensile specimen tested with a constant extension rate was observed with a SEM. Figure 8 shows that the fracture of the specimen is purely ductile.

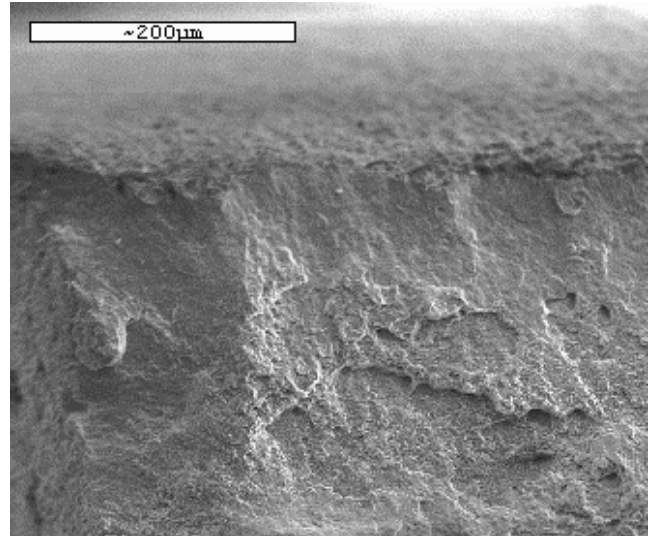


Figure 8 : Ductile fracture of the specimen after a CERT

SEM observation also reveals the occurrence of surface defects (figure 9). These shallow defects are similar to the ones observed at the apex of the U-Bends.

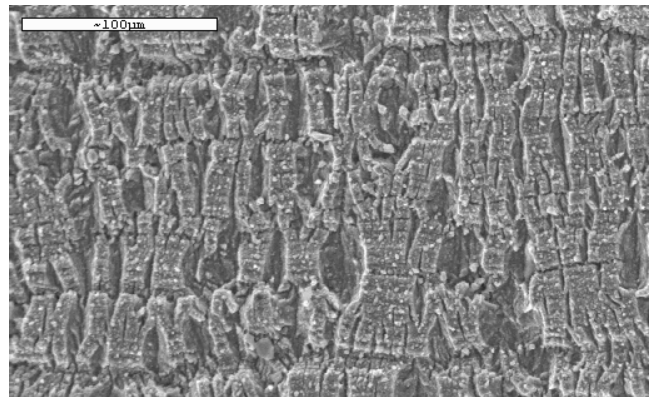


Figure 9 : Defects observed at the surface of the specimen after a CERT

The same test, but carried out in an inert medium (pure helium), was also performed in order to determine the origin of these shallow defects: purely mechanical defects or SCC cracks.

The same defects were observed at the surface of the specimen tested in the inert medium. The origin of these defects is thus purely mechanical in nature.

As for the U-Bends, the reasons why these defects appear in the cold worked layer are both the "low" ductility of the material and mainly the high level of deformation at the surface of the cold worked layer.

CONCLUSIONS

The tests performed in the framework of this study allow a better knowledge of the SCC resistance of EUROFER'97 in a hydrogenated aqueous medium. This program complements the program performed in the framework of the task SM3-3.

The tests performed, U-Bends tests and CERTs, show that this material has a good SCC resistance in the test medium. Complementary tests should be performed to assess the SCC of this material in polluted water, in presence for instance of dissolved oxygen and chloride.

The susceptibility of this material to hydrogen embrittlement should also be investigated.

REPORTS AND PUBLICATIONS

O. RAQUET, C. DUFOUR, L. SEJOURNE, "Stress Corrosion Cracking behaviour of EUROFER'97 in water with additives. Task TW1-TTMS-003-D12. Final Report" CEA report DEN/DPC SCCME 03-651-A, October 2003.

TASK LEADER

Olivier RAQUET

DEN/DPC/SCCME/LECA
CEA-Saclay
F-91191 Gif-sur-Yvette Cedex

Tél. : 33 1 69 08 15 92

Fax : 33 1 69 08 15 86

E-mail : olivier.raquet@cea.fr

TW2-TTMS-001b-D02**Task Title: IRRADIATION PERFORMANCE**
Neutron irradiation to 35-70 dpa at 325°C and PIE**INTRODUCTION**

The main objective of this experiment is to study the irradiation behaviour of Reduced Activation Martensitic steels at high doses and for irradiation temperatures lower than 400°C, where materials are susceptible to reach a high level of hardening and embrittlement.

For this purpose, irradiations experiments are conducted in the BOR60 reactor of the Research Institute of Atomic Reactors (RIAR, Dimitrovgrad, Russia) at 325°C.

This task includes two items:

- The Post Irradiation Examinations (PIE) corresponding to specimens irradiated in the first experiment (1st phase) in BOR60 that finished in 2002 for a target dose of about 35 dpa.
- A 2nd phase of irradiation in the same reactor for 40 dpa at the same temperature that will allow to reach in specimens already irradiated in the 1st phase a dose of 70-80 dpa.

The European reference Eurofer 97 (9Cr-1WTaV) RAFM steel, experimental heats type 9Cr-2WTaV and ODS Fe-Cr alloys are included in both irradiations.

2003 ACTIVITIES

The 1st phase irradiation experiment in the BOR60 reactor finished on October 2002. Specimens included in this experiment have reached a dose ranging from 32 dpa up to 42 dpa. PIE started in 2003 and are conducted in hot cells of RIAR. In the first half of 2003, the profilometry of pressurised tubes was completed. Because of some experimental problems in the hot cells, tensile tests were performed in the last quarter 2003. The treatment and interpretation of rough data is in progress. The 2nd phase of irradiation started in January 2003 and experiment runs according to the initial schedule.

MATERIALS / SPECIMENS

Materials irradiated in BOR60 are: Eurofer 97 (9Cr1WTaV), 9Cr2WTaV, 9Cr2WTaVB and ODS alloys. Chemical composition are given in [1]. The heat references and metallurgical conditions of these materials are presented on table 1.

RAFM steels, that is, Eurofer97, 9Cr-2WTaV and 9Cr-2WTaVB were produced as plates in the Normalized and Tempered (N&T) conditions.

ODS-MA957 ferritic alloy (Fe-14Cr-1Ti-0.3Mo) was produced as rod bars (8 mm in diameter) with two different microstructures constituted by: a) fine grains (0.5 microns size) obtained after a stress-relieved treatment (SR); b) recrystallised (R) grain structure (20-50 microns size) obtained with a particular fabrication route and a final recrystallisation treatment at 1100°C for 45 minutes.

Table 1 : References and metallurgical conditions of materials irradiated in Altair experiment

Material	Heat Number	Product Reference Nb	CEA reference	Final Heat Treatments
Eurofer 97	E83698 Böhler	Plate - 8mm n°66/5	931	N : 980°C – 27min. T : 760°C – 90 min.
9Cr-2WTaV	VS3104 British Steels	Rectangular bar - 25mm thick, n° 7	919	N : 1050°C – 60 min. T : 750°C – 120 min.
9Cr-2WTaVB	VS3224 British Steels	Rectangular bar- 25mm thick, n° 1-2	920	N : 1050°C – 60 min. T : 750°C – 120 min.
ODS – MA957 SR	CBB0108 INCO Alloys	Rod bar 8mm diam. FGT 2467	234i	Stress-relieved treatment : 920°C – 90 min.
ODS – MA957 R	JBB0151 INCO Alloys	Rod bar 8mm diam. FGT 3941	942	Recrystallisation treatment : 1100°C – 45 min.

Materials are irradiated as samples destined to mechanical tests. Three types of specimens are included:

- Tensile specimens of 2 mm in diameter and 12 mm of gauge length obtained in the transverse direction in the case of RAFM plates, along the axial direction for ODS alloys.
- Charpy subsize (KLST type) of 3 mm thick, 4 mm wide and 27 mm long machined with TL orientation for RAFM steels, LT for ODS.

Pressurized tubes of Eurofer 97 and 9Cr2W-TaV steels, for determination of in-pile creep. The dimensions of tubes are 6.55 mm and 5.65 mm respectively for the external and internal diameter and a total length of 55 mm. Tubes were machined in the transverse direction of plates. The junctions plug-tube were made by EB welding.

IRRADIATION EXPERIMENT (1ST PHASE)

The CEA irradiation experiment, named "Altair", was shared with other material project of CEA. Specimens for the Fusion programme occupied 30 % of the rig volume.

The rig of Altair was constituted of 7 levels or stages. The environment in the capsule was liquid sodium. The irradiation experiment was conducted over 12 irradiation cycles. The maximum neutron flux was reached at the level 3 (see figure 1 of ref [1]) and the instantaneous maximum flux of fast neutrons ($E > 0.1$ MeV) corresponding to this level was about $2.00 \pm 0.05 \times 10^{15}$ n.cm⁻² s⁻¹. The average temperature of irradiation changes from different cycles, but the average values were always within the requested range $325^\circ\text{C} \pm 5^\circ\text{C}$ for all levels.

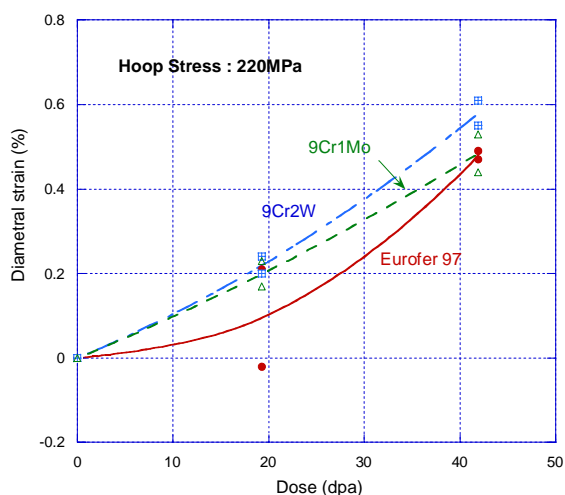


Figure 1 : Diametral strains measured for Eurofer 97 and 9Cr2W RAFM steels as a function of the dose for a hoop stress of 220 MPa. Values are compared to the behaviour of a commercial 9Cr1Mo martensitic steel irradiated in the same experiment

Tensile and Charpy specimens of Eurofer 97, 9Cr-2W and 9Cr2WB were located in stage 3, those of MA957 SR and MA957R in the stage 2 and 7 and the pressurized tubes in the level 1 as indicated in table 2, where dose levels correspond to the experimental values measured by neutron detectors.

Table 2 : Final doses attained by different types of specimens

Materials	Specimens	Level	Final dose
Eurofer 97 – 9Cr2W-TaV	Pressurized tubes	1	41.9
ODS / MA957 (SR)	Tensile & Charpy KLST	2	42.2
Eurofer 97 – 9Cr2W-TaV - 9Cr2W-TaVB	Tensile & Charpy KLST	3	42.3
9Cr2W-TaV – ODS / MA957 (R)	Tensile & Charpy KLST	7	32.5

PROFILOMETRY OF PRESSURISED TUBES

The objective of profilometry measurements of pressurised tubes is to determine the deformation due to in-pile creep. The argon pressure inside the pressurized capsules was adjusted to induce a hoop stress level of 150 and 220 MPa at the irradiation temperature.

This type of measurements has been performed before irradiation, at the intermediary dose of 19.3 dpa and after the final fluence of 41.9 dpa. The weight of each pressurised specimen is also measured at each step to guarantee that there is not leakage of argon pressure. Figure 1 shows the average diametral strains determined for EUROFER 97 and 9Cr2W-TaV RAFM steels compared to the 9Cr1Mo conventional martensitic steel. In all the cases, the strains measured are very low (≤ 0.6 %) after about 42 dpa, confirming the rather good dimensional stability of ferritic-martensitic steels.

To estimate the irradiation creep modulus, the following relation was used:

$$\varepsilon_{\theta} = 0.75 A \phi t \sigma_{\theta}$$

where ε_{θ} is the diametral strain, ϕt the dose, σ_{θ} the average hoop stress and A the irradiation creep modulus. Contributions from swelling and thermal creep are assumed negligible.

Values estimated for the creep modulus are $A = 0.4-1.0 \times 10^{-6}$ (dpa.Mpa)⁻¹, which are in good agreement with values already determined for ferritic-martensitic steels at high temperatures (400-550°C).

TENSILE TESTS

As rough data were received recently, the treatment of data is not yet available for all irradiated materials.

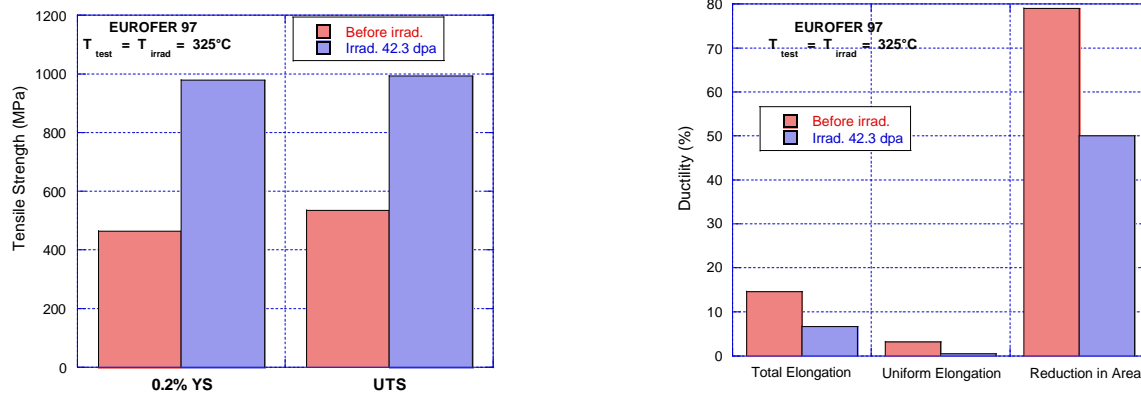


Figure 2 : Tensile properties of EUROFER 97 after irradiation at 325°C for a dose of 42.3 dpa

Figure 2 shows the preliminary results concerning the evolution of the tensile properties obtained for EUROFER 97 steel after irradiation at 325°C with a dose of 42.3 dpa. As expected, the tensile strength increases by a factor of about 2 with the associated decrease of ductility. However, the reduction in area values are relatively high showing that the material keeps enough ductility.

CONCLUSIONS / FUTURE WORK

PIE of specimens irradiated in “Altair” experiment performed in BOR60 started during 2003. Materials reached a radiation damage ranging from 32.5 to 42.3 dpa.

The preliminary results show that EUROFER 97 displayed a quite low irradiation-creep deformation. As expected, this material hardens during irradiation but it should keep a reasonable level of ductility.

Charpy tests to establish the energy transition curves are foreseen to be performed in 2004. The schedule depends on the installation of the impact machine in RIAR’s hot cells.

A fraction of specimens irradiated in Altair capsule are re-irradiated in the FZK/CEA common experiment Arbor 2, also performed in BOR60 reactor. This one started on January 2003 and reached in October 2003 a dose of about 12 dpa.

REPORTS AND PUBLICATIONS

A. ALAMO, J.L. BERTIN, “CEA irradiation experiment performed in BOR 60 reactor”, N.T. SRMA 03-2534, March 03.

TASK LEADER

A. ALAMO

DEN / DMN / SRMA
CEA-Saclay
F-91191 Gif-sur-Yvette Cedex

Tél. : 33 1 69 08 67 26

Fax : 33 1 69 08 71 67

E-mail : ana.alamo@cea.fr

Not available on line

TW2-TTMS-005b-D05

**Task Title: RULES FOR DESIGN, FABRICATION AND INSPECTION
Collection, qualification and presentation of mechanical properties
of Eurofer**

INTRODUCTION

Eurofer is a reduced activation ferritic / martensitic steel that has been selected as the European reference structural material for ITER Test Blanket Modules and DEMO reactor. Several industrial heats of this steel have been produced and tested under EFDA's Tritium breeding and materials field / materials development area tasks. The ultimate goal of these tasks is to propose materials properties allowables for design and licensing of components fabricated with the Eurofer steel.

TTMS-005 is one of the EFDA tasks that specifically targets structural materials rules, design and inspection. Its scope is extended since the year 2003 to include metallurgical and mechanical properties characterization actions that were previously carried out under TTMS-002.

This report presents a summary of the work done during the year 2003 at CEA for the deliverable 5 of TW2-TTMS-005b.

The primary objective of this deliverable is to collect, validate and harmonize the results of Eurofer steel, in continuation of the earlier work done on the conventional 9Cr-1Mmo steel and the RAFM steel grade produced in Japan (F82H).

2003 ACTIVITIES

The database of F82H steel was updated.

The new results reported for Eurofer steel were collected, analysed and when validated were added to the reference databases. This was a tedious job, since many associations had only provided hard copies of their results.

With the addition of the new Eurofer steel results, the databases have now:

- Product database: 571 records including 118 on Eurofer.
- Composition database: 475 records including 26 on Eurofer.
- Tensile database: 1018 records including 258 on Eurofer.
- Impact database: 1520 records including 467 on Eurofer.

- Impact plots: 161 records including 45 on Eurofer.
- Creep database: 205 records including 81 on Eurofer.
- Fatigue database: 112 records including 27 on Eurofer.

Fracture Toughness database: 78 records and Master curve files including 48 on Eurofer:

- Summary database of all above databases for heat, product and sub-products.

In addition to a major revision of the summary database that groups all the results together, in 2003 the fracture toughness database was extended to include master curve interpretation of results.

An example of the data sheet for a fracture test performed at CIEMAT on a CT specimen is shown in figure 1.

A CD-Rom with runtime solution v. 2 of the database was sent to the participating associations through EFDA.

The screenshot shows a software interface for a fracture test data sheet. It is divided into several sections:

- PRODUCT:** Alloy (F82H), Metal (Base), Designation (F82H_JEA), Manufacturer (NKK), Weight_kg (5000), Heat (9753), Product No (KG820-31), Sub-Product No (KG820-31W-3), CW% (0), Thick (mm) (25).
- HEAT TREATMENTS:** HT (C) (1040), HT (min) (40), Temper (C) (750), Temper (min) (60), PWHT (C) (), PWHT (min) (), Aging (C) (), Aging (h) (0).
- IRRADIATION:** State (N&T), Facility (), Experiment (), Irr_Medium (), Position in Rig (), Irr_T (C) (), Dose (dpa) (0), He_appm ().
- SPECIMEN:** No (31W-3-19), Sp. Type (CT), size (mm) (W: 50.8, B₀: 24, B: 24, s₀: 31.038, s₀/W: 0.611), Tensile at fatigue precrack Temp. (), Tensile properties at Test Temp. (), Fatigue Precracking ().
- TEST:** Source (JAERI), Country (Japan), Test No (), Method (), Analysis (), Environment (Air), Type control (), Displ. Rate mm/min ().
- RESULTS (K in MPa√m, J in KJ/m², a in mm, T in °C):** Data Set No (1), Test T (20), K_{IC} (348), K_{IC_1T} (), J_{IC} (297.1), J_{IC_2BL} (), J_{1mm} (), δ = A + C Δa^{3/2} (A: [], C: [], D: []), Δa (0.244), s_{0,est} (), s_{f,est} (), validity (No), K_{IC} Master Curve (), J_{max} (765), J_{IC} (), dJ/dΔa (MPa) (), J = A + C Δa^{3/2} (A: [], C: [], D: []).
- Observations:** TIG Joint
- References:** JAERI/Striba

At the bottom, it shows 'date: 8 January 2004', 'RAFM Fracture Detail for Record: 2', and 'page: 1'.

Figure 1 : Example of a fracture data sheet

CONCLUSIONS

Presently the reference databases contain sufficient data on unirradiated tensile and creep properties for a reliable estimation of design allowables for these properties. This is also the case of impact toughness, where data for standard and sub-size specimens taken from various products in different orientations, before and after thermal ageing is significant. The available data on fatigue and fracture toughness are still limited. Likewise, the data on irradiated materials is sparse.

Additional work in the above areas is needed.

REPORTS

- [1] A.-A.F. Tavassoli, Revision 2, Interim Appendix A Materials Design Limit data for A3.S18E Eurofer steel, Interim TTMS 5.5 & 5.9 reports, N.T. CEA/DEN/SAC/DMN June 2003.
- [2] Runtime solution of the RAFM databases, V. 2, CD-Rom, 2003.
- [3] A.-A.F. Tavassoli, et al, Materials design data for reduced activation martensitic steel type Eurofer, ICFRM-11, session 6A, Kyoto, Japan, Dec. 7-12, 2003.

TASK LEADER

Farhad TAVASSOLI

DEN/DMN
CEA-Saclay
F-91191 Gif-sur-Yvette Cedex

Tél. : 33 1 69 08 60 21
Fax : 33 1 69 08 80 70

E-mail : tavassoli@cea.fr

TW2-TTMS-005b-D09

Task Title: RULES FOR DESIGN, FABRICATION AND INSPECTION
Material design limits for TBM's application: Update and completion of
Appendix A for Eurofer steel including new heats

INTRODUCTION

Eurofer steel is a reduced activation ferritic/martensitic steel that has been selected as the European reference structural material for ITER Test Blanket Modules and DEMO reactor. Several industrial heats of this steel have been produced and tested under EFDA's Tritium breeding and materials field / materials development area tasks. The ultimate goal of these tasks is to propose materials properties allowables for design and licensing of components fabricated with the Eurofer steel.

TTMS-005 is one of the EFDA tasks that specifically targets structural materials rules, design and inspection. Its scope is extended since the year 2003 to include actions previously carried out under the TTMS-002 task (Metallurgical and mechanical characterisation).

This report presents a summary of the work done during the year 2003 at CEA under the deliverable 9 of TW2-TTMS-005b. The primary objective of the work is to update and complete the Appendix A (similar to RCC-MR) for the Eurofer steel.

2003 ACTIVITIES

The data generated under the deliverable TW2b-TTMS 005-D5 were used to determine the materials properties allowables for Eurofer steel.

Revision 2 of the interim Appendix A Materials Design Limit data for A3.S18E Eurofer steel was issued. This report covers, in addition to the mechanical properties, the physical properties of Eurofer, including magnetic properties. However, it misses Eurofer properties such as coefficient of thermal expansion and Young's modulus, for which new actions are now launched. In the meantime data from the conventional 9Cr-1Mo steel and F82H steel are used.

The Appendix A for 9Cr-1Mo, F82H and Eurofer steels were also included in the runtime solution v. 2 of the RAFM databases that was sent to EFDA.

CONCLUSIONS

The database for Eurofer steel is progressing. Most of the conventional design limits can be derived with adequate reliability and used for the ITER test blanket modules where anticipated irradiation doses are moderate. Additional work is needed to substantiate fatigue and fracture toughness databases and in all cases for higher dose irradiations.

REFERENCES

- [1] A.-A.F. Tavassoli, Revision 2, Interim Appendix A Materials Design Limit data for A3.S18E Eurofer steel, Interim TTMS 5.5 & 5.9 reports, N.T. CEA/DEN/SAC/DMN June 2003.
- [2] Runtime solution of the RAFM databases, V. 2, CD-Rom, 2003.
- [3] A.-A.F. Tavassoli, et al, Materials design data for reduced activation martensitic steel type Eurofer, ICFRM-11, session 6A, Kyoto, Japan, Dec. 7-12, 2003.

TASK LEADER

Farhad TAVASSOLI

DEN/DMN
CEA-Saclay
F-91191 Gif-sur-Yvette Cedex

Tél. : 33 1 69 08 60 21
Fax : 33 1 69 08 80 70

E-mail : tavassoli@cea.fr

Not available on line

Not available on line

Not available on line

Not available on line

Task Title: MODELISATION OF IRRADIATION EFFECTS
Ab-initio calculations of the system Fe-He

INTRODUCTION

Under fusion relevant conditions, low activation steels are exposed to intense irradiation by 14 MeV neutrons which produce defects induced by displacement cascades (vacancies, interstitials, as well as vacancy and interstitial clusters) but also helium and hydrogen atoms by transmutation. The effect of helium, in particular when combined with vacancies, on microstructural evolution is one of the specificities of the behaviour of these materials, which requires quantitative predictions, in particular by modeling tools.

The objective of this subtask is to provide a database at the *ab-initio* level, i.e. in the framework of the Density Functional Theory (DFT), of energies and structures for a set of characteristic atomic configurations involving helium atoms and vacancies in the α -Fe lattice.

The applications of these data are threefold: they can be used (i) either directly for a better characterisation of small helium-vacancy (He-V) complexes in α -Fe ; (ii) or as input data in a kinetic model for defect population evolution (e.g. Monte Carlo - or Rate Theory) ; (iii) or as input data for the fit of semi-empirical interatomic potentials, that can in turn be used for the simulation of larger He-V clusters and/or for molecular dynamics simulations.

2003 ACTIVITIES

We have set up a methodology for the *ab-initio* calculation of the energetics of helium-vacancy defects in α -Fe based on the SIESTA DFT-code (Spanish Initiative for Electronic Simulations with Thousands of Atoms: <http://www.uam.es/siesta>) [1].

We have first developed a pseudopotential and a basis set for He. This calculation scheme has then been validated on helium insertion calculation by comparison with reference calculations, based on plane-wave basis sets. This validation, as well as the first results on small helium-vacancy complexes are presented below. All calculations are performed in the General Gradient Approximation (GGA).

He INSERTION

The SIESTA method is first validated for calculations of He defects in the α -Fe matrix by comparison with results obtained using the PWSCF planewave-pseudopotential code. The comparison is performed on the insertion energy of He in α -Fe, calculated in 27-atom cells at constant supercell volume for following configurations: substitutional, tetrahedral and octahedral (see figure 1).

The insertion energies, $E_{S,T,O}^I$, are calculated as follows:

$$E_S^I = E((N-1) Fe_{Fe}, He_{Fe}) - \frac{N-1}{N} E(N Fe_{Fe}) - E(He) \quad (1)$$

and

$$E_{T,O}^I = E(N Fe_{Fe}, He_{T,O}) - E(N Fe_{Fe}) - E(He) \quad (2)$$

where for instance $E((N-1) Fe_{Fe}, He_{Fe})$ is the energy of a cell with (N-1) Fe atoms on Fe sites and one He atom on a Fe site. Indexes T and O indicate octahedral and tetrahedral sites, and $E(He)$ is the reference energy for He atoms, taken here in the solid hcp structure.

The results presented in table 1 show that the agreement between the two methods is excellent: the SIESTA basis sets for Fe and He are therefore fully validated for this type of calculations. In the following, only the SIESTA method will be used.

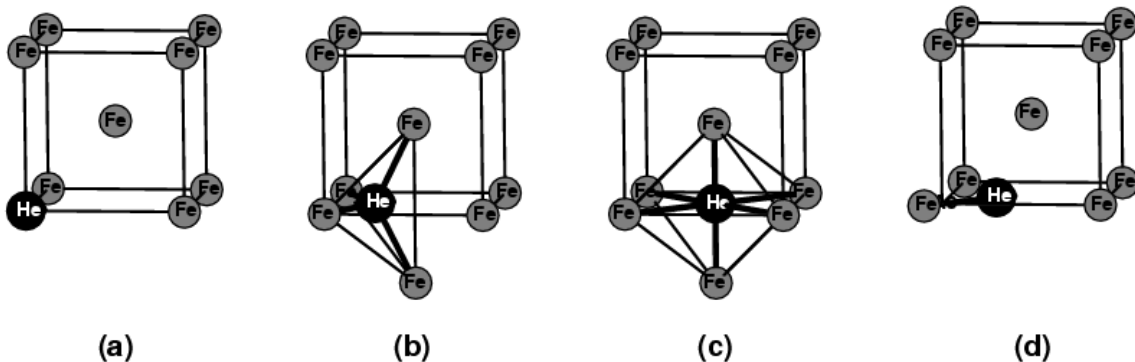


Figure 1 : Schematic representation of the configurations investigated here for the insertion of He in α -Fe :
(a) substitutional, (b) tetrahedral, (c) octahedral and (d) mixed <110> dumbbell

Table 1 : Insertion energy of He in α -Fe (in eV) :
 (1) PWSCF/SIESTA comparison for a calculation at constant supercell volume with 27 sites ; and
 (2) SIESTA calculation at constant pressure with 54 atoms. The energy differences
 with respect to the most stable configuration (substitutional) are indicated in parentheses.

	Substitutional	Tetrahedral	Octahedral	<110> mixed dumbbell
PWSCF-27_V	4.26 (0.0)	4.53 (0.37)	4.87 (0.61)	/
SIESTA-27_V	4.13 (0.0)	4.55 (0.42)	4.74 (0.61)	/
SIESTA-54_P	4.06 (0.0)	4.32 (0.26)	4.50 (0.44)	4.39 (0.33)

After validation on constant-volume calculations with 27-atom cells, the final results are obtained by repeating the same calculations on larger cells (54 atoms) at constant pressure. An additional configuration, namely the <110> mixed dumbbell (see figure 1 (d)) is investigated. The results are reported in table 1. From the comparison with the 27-atom constant-volume calculations, it can be concluded that the present results are well converged with respect to supercell size. The results that are obtained are quantitatively and qualitatively different from previous predictions by empirical potentials [3]:

- The order of stability is: substitutional, tetrahedral (+0.26 eV), <110> mixed dumbbell (+0.33 eV), and octahedral (+0.44 eV). The energy difference between substitutional and interstitial (0.26 eV) is much smaller than with empirical potentials (2 eV).
- The solution enthalpy of substitutional He is 4.1 eV (instead of 3.25 eV with empirical potentials).
- The binding energy between a vacancy and a tetrahedral interstitial He atom is 2.33 eV (instead of 3.7 eV with empirical potentials). It is deduced from the sum of the vacancy formation energy, 2.07 eV, and $E_T^I - E_S^I$.
- According to these results, the following conclusions can be drawn for the behaviour of helium atoms in α -Fe, and its interaction with vacancies:
- At equilibrium, helium atoms have a substitutional configuration.
- When He atoms are produced in the bulk (e.g. by transmutation), their metastable configuration (before reacting with vacancies or other defects or defect clusters) is tetrahedral interstitial. This result is at variance with empirical potential predictions giving the octahedral configuration.
- From the small value of the energy difference between tetrahedral and octahedral configuration, a very low value is expected for the migration energy of interstitial He.
- As expected, interstitial He atoms and vacancies are highly attractive. This attractive interaction is the driving force for the formation of helium-vacancy clusters.

He₂V AND HeV₂ COMPLEXES

As a first step towards the formation of small helium-vacancy complexes, we have then investigated the relative stability of various configurations for He₂V and HeV₂ complexes. For the He₂V complex, the three dumbbell orientations are found to have nearly the same energies: the <100> and <111> configurations are 0.04 eV lower than the <110> one (see figure 2). Our results suggest that the He₂ dimer has a nearly free rotation inside the vacancy and that it may exhibit large amplitude vibrations.

For the He–divacancy complex (HeV₂) both for the nearest-neighbour (NN) and the next-nearest neighbour (NNN) configurations have been investigated. In both cases (NN and NNN), the complex is more stable when the He atom is mid-way between the two vacancies. It is also the case for empirical potentials but only for the NN case [3].

The configurations where one vacancy is filled with an He atom and the second one is empty are even unstable for NN and NNN vacancies. They become stable only for third nearest neighbour vacancies. The NN configuration is more stable than the NNN one (by 0.4 eV), unlike without He, where the NNN is more stable by 0.1 eV.

A deeper insight into the formation of these complexes can be gained by determining the energy balance of their formation reaction starting from a smaller complex and an isolated vacancy or tetrahedral interstitial He atom. All these reactions are found to be exothermic. The binding energy between a vacancy and a He_nV_{m-1} cluster can be defined as:

$$E_B(V) = E([N-(m-1)] \text{ Fe}, n \text{ He}) + E((N-1) \text{ Fe}) - E((N-m) \text{ Fe}, n \text{ He}) - E(N \text{ Fe})$$

where $E((N-m) \text{ Fe}, n \text{ He})$ is the energy of the system with (N-m) Fe atoms and a He_nV_m cluster. The binding energy of an interstitial tetrahedral helium atom with a He_{n-1}V_m can be defined in a similar way as:

$$E_B(\text{He}) = E((N-m) \text{ Fe}, (n-1) \text{ He}) + E(N \text{ Fe}, \text{He}) - E((N-m) \text{ Fe}, n \text{ He}) - E(N \text{ Fe})$$

The convention adopted here is a positive sign for an attraction between the vacancy or the helium atom and the initial He-V cluster.

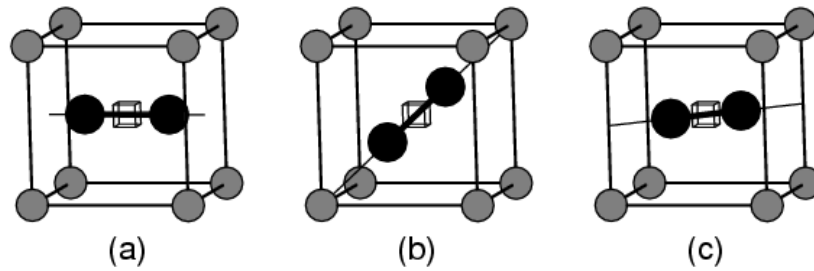


Figure 2 : Schematic representation of the most stable configurations found for He_2V complexe, with the He_2 dimer (in black) in the : (a) $\langle 100 \rangle$, (b) $\langle 111 \rangle$, or (c) $\langle 110 \rangle$ directions. The He atoms (in black) are represented at their positions after relaxations, while the Fe atoms (in grey) are left on the perfect lattice positions. The vacancy is represented by a small cube

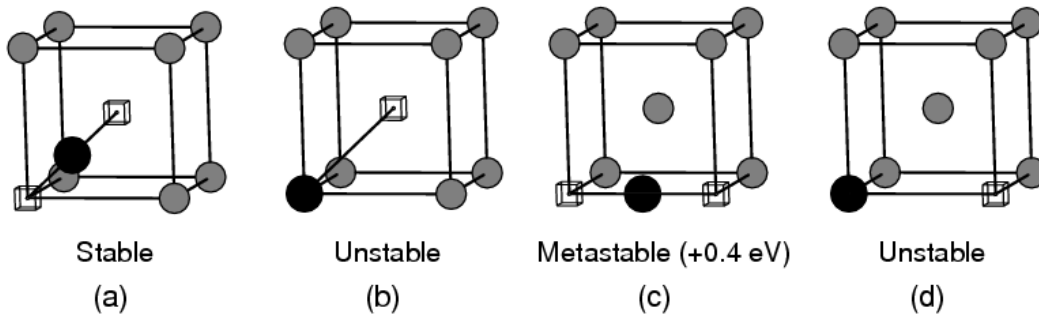
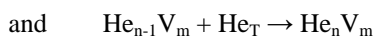


Figure 3 : Schematic representation of the nearest neighbour (NN) and next nearest neighbour (NNN) configurations investigated here for HeV_2 complexes: with the He atom midway ((a) and (c)) or in one of the vacancies ((b) and (d)).

Table 2 : Calculated properties of He insertion and He-V interactions in α -Fe : comparison between *ab-initio* (present work) and empirical potential predictions (Ref. [3]). The binding energies of He atoms with He-V clusters refer to interstitial He atoms.

Property	<i>Ab-initio</i>	Empirical potential
He insertion energy	4.06 eV	3.25 eV
He interstitial site	Tetrahedral	Octahedral
Insertion energy difference (interstitial – substitutional)	0.26 eV	2.0 eV
He-V binding energy	2.33 eV	3.70 eV
He- V_2 binding energy	2.87 eV	3.98 eV
V-HeV binding energy	0.65 eV	0.46 eV
He-HeV binding energy	1.82 eV	/

They correspond respectively to the reactions:



where He_T is an interstitial tetrahedral helium atom. The calculated binding energies are summarized in table 2.

The comparison with previous predictions by empirical potentials shows quantitative and qualitative differences.

CONCLUSIONS

We have successfully set up an *ab-initio* calculation scheme for the study of helium-vacancy defects in α -Fe, using the SIESTA code in the DFT-GGA framework. This methodology has been validated on reference configurations by comparison with plane wave pseudopotential calculations. A first set of results has been obtained on the insertion of helium in α -Fe.

The calculations performed on 54-atom supercells at constant pressure show that: (i) the substitutional configuration is the most favourable; (ii) the most stable interstitial configuration, i.e. the metastable configuration for He atoms when they are produced in the bulk by transmutation, is tetrahedral and (iii) the binding energy between a vacancy and an interstitial helium atom is 2.3 eV. As a first step towards the study of the formation of helium-vacancy clusters, this scheme has then been applied to the study of He₂V and HeV₂ clusters. For He₂V, the energy is found to be nearly independent on the orientation of the He₂ dimer inside the vacancy (<100>, <111> or <110>).

For first and second nearest neighbour HeV₂ clusters, the He atom is midway between the two vacancies and it stabilizes the nearest-neighbour configuration (unlike in the case without He). The impact of using a more accurate ab-initio approach rather than existing empirical potentials is summarized in table 2. It can be seen that the major discrepancy is the relative stability of substitutional and interstitial He, which differs by almost one order of magnitude between the two types of calculation. Completing this ab-initio database should help fitting new empirical potentials, which in turn will allow studying larger He-V clusters as well as dynamical effects.

REFERENCES

- [1] J.M. Soler, E. Artacho, J.D. Gale, A. Garcia, J. Junquera, P.Ordejon and D. Sanchez- Portal, J. Phys. Cond. Matter **14**, 2745 (2002).
- [2] C.C. Fu, F. Willaime and P. Ordejon, submitted for publication.
- [3] K. Morishita et al., Proc. 4th Pacific Rim. Int. Conf.on Advanced Materials and Processing (PRICM4), Hawaii, USA, (2001), The Japan Institute of Metals, p. 1395 ; K. Morishita, private communication.

REPORTS AND PUBLICATIONS

F. Willaime and C.C. Fu, Ab initio calculations of helium-vacancy defects in α -Fe: first results, CEA report DEN/DMN/SRMP/2004-002/I, February 2004.

TASK LEADER

François WILLAIME

DEN/DMN/SRMP
CEA-Saclay
F-91191 Gif-sur-Yvette Cedex

Tél. : 33 1 69 08 43 49
Fax : 33 1 69 08 68 67

E-mail : fwillaime@cea.fr

Task Title: SiC/SiC CERAMIC COMPOSITES
Study of a multi-scale model to simulate the mechanical behaviour of SiC_f/SiC composite

INTRODUCTION

The final aim of this study is to model the thermo mechanical behaviour of SiC_f/SiC as structural material for fusion reactor in order to test the different designs and to evaluate their resistance under thermal and mechanical loadings corresponding to normal or accidental scenarios.

The literature review performed in 2003 indicates that because of the mechanical and structural characteristics of this composites, the most promising way to obtain a reliable behavioural model that can evolve with our knowledge of the material is to use multi-scale modelling.

2003 ACTIVITIES

A literature review was performed. The mechanical behaviour SiC_f/SiC is non linear elastic at low temperature and controlled by damage. At high temperature, SiC_f/SiC can moreover creep.

The present work focus on damaging behaviour but it can be extended to visco-plastic behaviour in the future since some of the homogenisation tools necessary to multi-scale modelling remain the same.

Damage consists in matrix micro-cracking, fibre matrix decohesion, fibre breaking and also loose of contact between matrix and fibre due to fibre shrinkage under irradiation. It therefore appears and develops at the matrix and fibre scale.

The study of the composite at this scale, referred to as micro mechanics, will allow a more physical description of the material behaviour. From the analyse of the arrangement and the properties of these phases, a homogenisation treatment allows to deduce the macroscopic homogeneous behaviour which can be used in a FE code. It is of an appreciable interest in the case of a material still under development and especially for a composite for which characterisation tests are complex, due to the coupling terms resulting from anisotropy.

The thermodynamic and dissipation potentials of the constituents are the bases of the micro-mechanical models. The thermodynamic potential defines the damage variables and the way they affect the elastic properties while the dissipation potential allows determining the damage kinetics. The strain-stress model of the damaged material (or the damaged phase) is entirely determined by the knowledge of these two potentials.

These potentials can be expressed in different ways following the phenomena and mechanisms that are considered to be the more relevant for the thermo-mechanical behaviour.

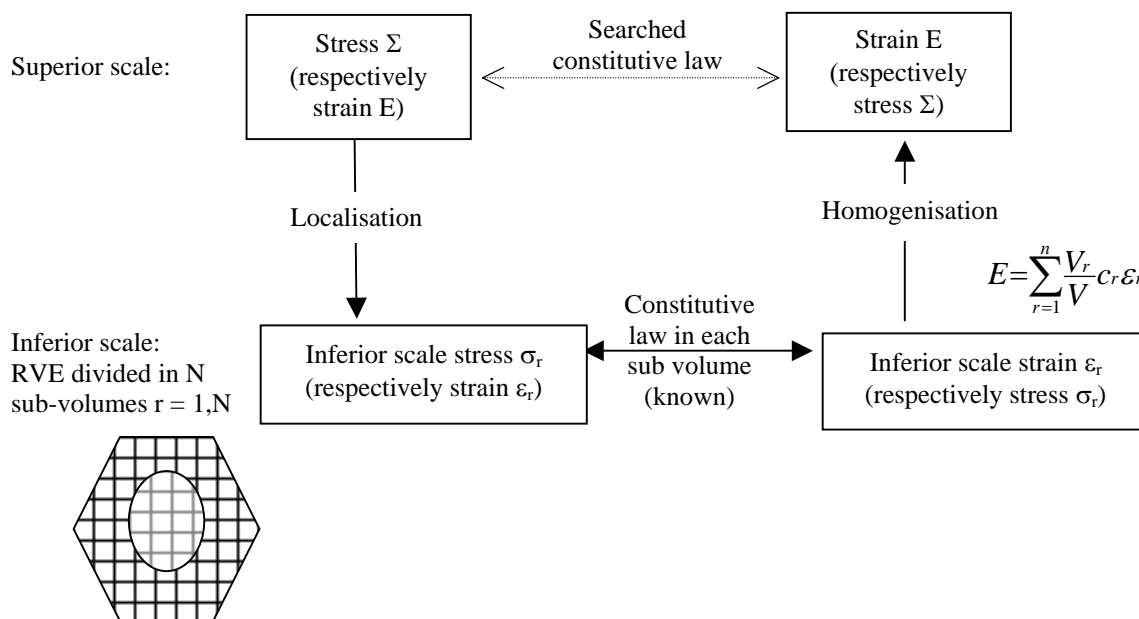


Figure 1 : Scale change principle

Moreover, scale change methods have to be chosen carefully depending on the behaviour of the constituents and the structure of the material. These methods allow to describe the macroscopic behaviour from the description of the microscopic behaviour.

For each scale change between a superior scale to an inferior scale three successive steps are necessary:

- The representation step: definition of a representative volume element (RVE) at the lower scale.
- The localisation step: local fields are obtained from the global fields.
- The homogenisation step: global fields are obtained from volume averages of the local fields.

These 2 last steps are illustrated on figure 1.

In the case of SiC_f/SiC two successive scale change are necessary, one from the macro (structure) to the meso scale (plies) step and one from the meso to the micro scale (fibre, matrix, interface).

The conclusions of the bibliography and of the meeting with specialists indicate that two different promising sets of formulations for the potentials could be adopted. The first one was proposed by Rospars et al [1] [2] who applied it successfully to modelling of SiC_f/SiC structures.

The second one could be developed from the bases of the work performed on this composite at the ONERA [3] [4]. The most adapted change scale methods have also been identified.

REFERENCES

- [1] C. Rospars, E. Le Dantec and F. Lecuyer, CMC damage prediction by micro-macro modelling, twelfth international conference on composite materials, Paris, France, 5th-9th (july 1999), ICCM-12.
- [2] C. Rospars, E. Le Dantec and F. Lecuyer, Composites Science and Technology 60 (2000) 1095-1102.
- [3] J. F. Maire and J. L. Chaboche, Aerospace Science and technology, 6 (2002), 131-145.
- [4] J. F. Maire and J. L. Chaboche, Aerospace Science and Technology, 1997, n°4, 247-257.

REPORTS AND PUBLICATIONS

C. Guerin, Multi-scale modelling for SiC_f/SiC composites, Preliminary considerations to an implementation in CAST3M, CEA report DRN/DMT SEMT/LM2S/RT/04-001/A, January 2004.

TASK LEADER

Caroline GUERIN

DEN/DMT/SEMT/LM2S
CEA-Saclay
F-91191 Gif-sur-Yvette Cedex

Tél. : 33 1 69 08 53 52
Fax : 33 1 69 08 86 84

E-mail : cguerin@cea.fr

Task Title: IRRADIATION OF SiC/SiC CERAMIC COMPOSITES AND TUNGSTEN ALLOYS

INTRODUCTION

The objective of these tasks is to irradiate in a common rig SiC-SiC ceramic composites and tungsten alloys samples at two temperatures, i.e., 1000°C and a lower temperature approximately of 600-650°C.

The dose foreseen is about 5 dpa equivalent Fe. This irradiation experiment will be performed in the Osiris reactor at CEA-Saclay.

The first step of this work consists on the design of the corresponding irradiation capsule based on the requirements defined by EFDA for this irradiation experiment, i.e., conditions required, fluence level, temperature distribution, materials, type, number and dimensions of specimens.

As said before, two families of materials are planned to be irradiated in this experiment, that is, several types of SiC_f/SiC ceramic composites and refractory tungsten-based alloys. All materials will be supplied by EFDA as machined specimens ready for irradiation.

2003 ACTIVITIES

Activities performed during this period were mainly focused on the design of the irradiation rig. Also, the preliminary design of the bunker with all the gas circuits was carried out as well as the first safety analysis, which has been approved by the safety committee.

It was agreed to name this experiment “FURIOSO” (FUSion RIg OSiris irradiatiOn).

IRRADIATION RIG

The irradiation capsule will be constituted of two sections of the same length, one that will work at 1000°C and the other in the range 600-650°C. Consequently, the calculation and drawing of a powerful furnace were performed to guarantee the good control of the temperature of specimens during irradiation. Inside the capsule, samples will be in contact with a gas mixture constituted of helium and neon, where the pressure on the samples should be lower than 6 bar. Figure 1 shows a preliminary design corresponding to the cross-section of the sample’s holder or basket, where the diameter is 24 mm.

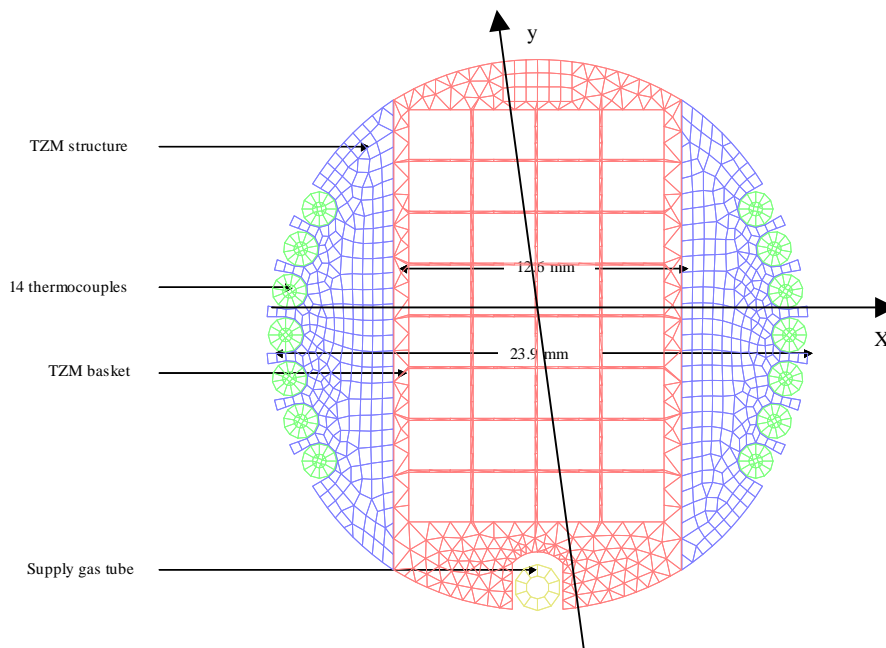


Figure 1 : Cross-section of a basket showing the location of samples, thermocouples and gas tube supply. Calculations of temperature distributions were performed along the “x” and “y” directions indicated

As the final loading plan is not yet defined, the first design is carried out assuming that samples have the following dimensions : 2 mm thick, 2.5 mm wide and 40 mm long. Specimens will be located in each one of the 32 positions shown in figure 1. The monitoring of temperature will be performed with thermocouples located in the periphery of the basket.

Calculations aim at maximising the volume allowed to samples and to minimise the temperature gradients in radial and axial directions.

The temperature gradients along the radial directions were evaluated assuming that baskets are loaded with: a) only SiC/SiC samples, b) only W samples or c) mixed loading W+SiC/SiC (8 SiC/SiC samples in the central positions).

Calculations were carried out along 2 axis “x” and “y” (not perpendicular between them) to estimate the real temperature of samples and considering the maximum neutron flux (and the maximum gamma flux too) of the reactor.

Figures 2 to 5 display the first estimates of the radial distribution of temperatures for the situations a) SiC/SiC loading and c) mixed 8 SiC/SiC + W samples.

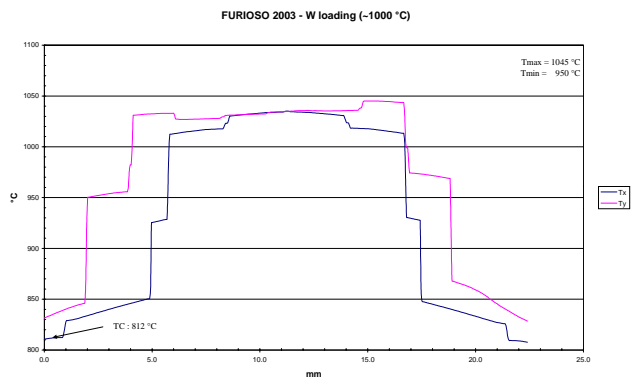


Figure 4 : Temperature distribution obtained in the case of a sample holder filled up with 8 specimens of SiC/SiC located in the central positions and the reminding ones with W-specimens, for a nominal temperature of 1000°C

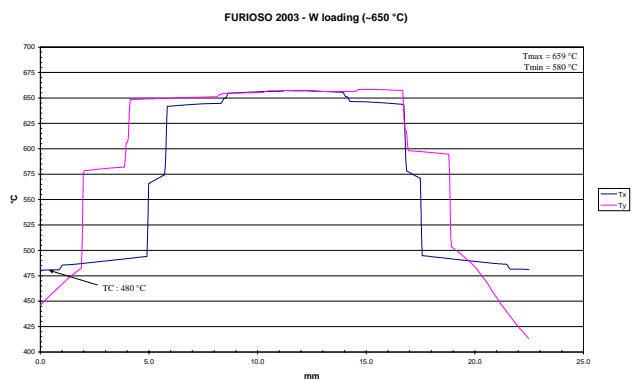


Figure 5 : Temperature distribution obtained in the case of a sample holder filled up with 8 specimens of SiC/SiC located in the central positions and the reminding ones with W-specimens, for a nominal temperature of 650°C

FURIOUSO 2003 - SiC Loading (~1000°C)

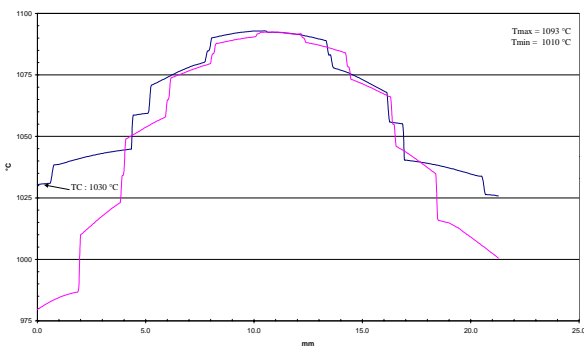


Figure 2 : Temperature distribution obtained in the case of a sample holder filled up with SiC/SiC specimens for a nominal temperature of 1000°C

FURIOUSO 2003 - SiC loading (~650°C)

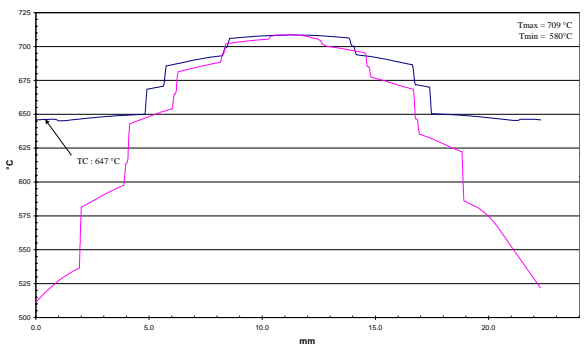


Figure 3 : Temperature distribution obtained in the case of a sample holder filled up with SiC/SiC specimens for a nominal temperature of 650°C

For the assumed configurations, the difference in temperature between samples located in the central and external positions is around +/- 50°C of the nominal temperatures (1000°C and 650°C) in the case of SiC composites and the mixed SiC/SiC + W samples.

If the whole loading is constituted by W-samples, the gradients obtained were very high (> 100°C) for the conditions considered.

FUTURE WORK

Calculations will be continued in order to minimise the gradient of temperature between samples located in the central positions and those near the periphery of the basket.

Distribution of temperature is strongly dependent on the type of material, number and dimensions of samples.

So, the definition from EFDA of loading plan is expected to be available very soon in order to perform the definitive design of the rig.

REPORTS

S. Bendotti, “ Material irradiation specifications - High Temperature Irradiation of SiC/SiC & W in OSIRIS - FURIOSO (FUSion RIg OSiris irradiatiOn) PROJECT”

- DRSN/SIREN/CIDI/CDC/532 for W-SPECIMENS
- DRSN/SIREN/CIDI/CDC/533 for SiC/SiC- SPECIMENS

TASK LEADER

A. ALAMO

DEN / DMN / SRMA
CEA-Saclay
F-91191 Gif-sur-Yvette Cedex

Tél. : 33 1 69 08 67 26
Fax : 33 1 69 08 71 67

E-mail : ana.alamo@cea.fr

Task Title: IFMIF, ACCELERATOR FACILITY
Development of critical accelerator components: Electron Cyclotron Resonance (ECR) source/Low Energy Beam Transport (LEBT) system

INTRODUCTION

INTRODUCTION AND BACKGROUND

The task was completed in the framework of the CEA program on high-power particle accelerators supported by the IPHI demonstrator project [1]. This project is dedicated to high power beam production (CW beam, 100 mA).

The injector system (source and Low Energy Beam Transport) must demonstrate reliability commensurate the maintenance schedule of the IFMIF accelerators. Low to very low spark rates have to be shown, as well as reliability in terms of source performances.

Very good beam quality has to be provided in order to ensure proper beam transport in the next accelerator sections. The ECR type of sources was selected for the IFMIF accelerator.

The task consists in experimental demonstration of D and H_2^+ ions extraction improvement, maximum performance and reliability of the system (reference concept); optimization of H_2^+ production for conditioning and facility testing. The activity specific to IFMIF has been concentrated on:

- Deliverable 1a: Development of critical accelerator components: ECR source/LEBT system.
- Deliverable 1b: Development of diagnostics for high power CW.

SUBDELIVERABLE 1A: ECR SOURCE DEVELOPMENT

Source reliability test

Beam characteristics and source behaviour have to be recorded and compared with a reduce beam current in order to have a better understanding of the availability process. This describes the so called “over-design” process. Statistics of the over-designed principle was conducted with a lower beam current (30 mA) and compared to the 120 mA statistics. To obtain low intensity beam the source was set with a 4.8 mm diameter extraction aperture. With this plasma electrode, the plasma density remains quite constant and the species fraction do not change.

At 30 mA, some current instability was observed, but no beam interruption over the sampling time was observed.

Previous high intensity reliability tests demonstrated source availability always higher than 95 %. Two runs of more than 100 hours showed higher than 99.8 % reliability. A new one-week test (162 hours) with a 110 mA – 95 keV beam has been performed. As previously observed, an average of 3 or 4 plasma extinctions led to 2.5 min beam interruption each day. The Mean Time To Repair (MTTR) was 2.5 min and the maximum time between failures was 28 hours. The achieved availability reached 99.3 %.

Neutron production in the LEBT

Low intensity deuteron beam has been produced for neutron emission measurements. The source was equipped with a small diameter (4.8 mm) extraction system to limit the intensity. A 5 mA – 40 keV CW Deuteron beam was produced. The neutrons were measured online with a LB 6411 probe. We were under a permanent control of the radiation safety service for this neutron measurement test. This experiment allowed acquiring data on 2.45 MeV neutron emission from (d,D) reaction.

The source worked in deuteron for 4 days. A maximum neutron production saturated dose of 420 μSv was observed. The preliminary conclusions of the measurements are as follow:

- The neutron emission appears isotropic around the copper target and follows the $1/d^2$ decay rule.
- After the start of the beam, the neutron emission rise time is rather short and reaches a saturation level.
- The saturation level linearly depends on the intensity of the beam.
- The neutron emission rise time depends on deuteron energy and beam intensity.
- The neutron emission rise time is about 1 hour with a 5 mA-40 keV deuteron beam on cleaned target and shorter after a beam restart on deuterium polluted target.
- The neutron emission fall time is very short when the beam stops (from 415 to 25 $\mu\text{Sv}\cdot\text{h}^{-1}$ after 6 min and 0.5 $\mu\text{Sv}\cdot\text{h}^{-1}$ after 30 min).

IFMIF H_2^+ measurements with the SILHI ECR source

IFMIF is foreseen to accelerate deuteron beams (2 x 125 mA) at 40 MeV for material behaviour investigation. The H_2^+ ions acceleration would help the commissioning of such a high intensity deuteron facility, especially by limiting neutron production before the industrial running mode.

The source has been designed and developed to maximize the atomic ions H^+ or D^+ intensity. Routinely the atomic ion fraction is higher than 80 % by adjusting the parameters with an optimized set up. The following possible actions to produce high H_2^+ current were:

- (i) Tuning of the magnetic configuration.
- (ii) Modify the injected RF power and/or H_2 gas pressure.
- (iii) Mix some gases (Ar, Xe, Ne, N_2 , H_2O , CO_2 for example).

First measurements have been performed by tuning the magnetic configuration. For each source set of parameters, the species fraction and the extracted intensity are recorded. The H_2^+ fraction increases while the extracted beam intensity decreases. It does not depend on the magnetic configuration; it continuously ranges from 15 to 21 %, with the different magnetic set up while the current goes down from 100 to 78 mA.

Other measurements, achieved by changing the injected hydrogen gas flow, led to a variation of the pressure into the plasma chamber (see figure 1). With hydrogen flow lower than 2.5 sccm, the RF power has been dramatically increased to maintain an almost constant extracted current (70 mA total). In spite of everything, in these conditions the extracted beam becomes instable.

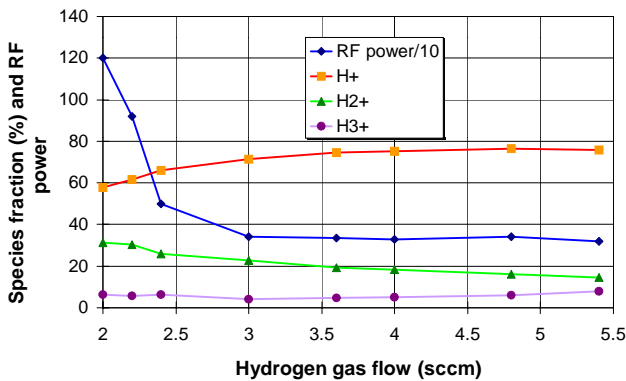


Figure 1 : Species fraction versus hydrogen gas injection

To stabilize the beam and improve the H_2^+ production, several mixing gas injections have been tested with no significant improvement on the molecular ion intensities. We tested unsuccessfully Ar, Ne, N_2 , H_2O and CO_2 . An important degradation of the beam characterized was observed by a dramatically drop of the intensity and an important increase of the heavy ion fraction. The stability of the source was also affected. This occurs with the injection of a very small CO_2 amount. As a result, the H_2^+ fraction does not change (relatively) but finally the total amount of H_2^+ ions decreases.

Conclusion

The above reported results do not show any important H_2^+ ion fraction improvement by changing the source parameters. So to conclude, one can expect a maximum H_2^+ current equal to 30 mA with a total 150 mA extracted beam.

This means some adaptation in the LEBT, in order to avoid degradation of equipment with such a high power deposition in the line. Of course no measurements compare D^+ and H_2^+ emittances during this campaign and we cannot ensure such a molecular beam could be sufficient for the IFMIF accelerator commissioning.

One may think of other commissioning possibilities, like debugging the accelerator with H^+ current (in order to verify the right quadrupole focalisation, for instance), and to quickly switch to D^+ beam, with a low current and a low duty cycle. The different options will have to be discussed among the accelerator team.

The design of a dedicated source for H_2^+ production is therefore highly recommended if IFMIF maintains the need of H_2^+ .

SUBDELIVERABLE 1B: BEAM DIAGNOSTICS

The continuous development of diagnostics was mainly attached to the Doppler shifted profile measurement, useful as a non interceptive measurement, and the wire scanner.

The scanner wire was designed, built and tested with success, in pulsed mode since it is an interceptive diagnostics. The beam energy deposition prohibits CW wire scanner analysis.



Figure 2 : Picture of the scanner wire

The mechanical resistance of the wire was tested, the electronic was validated, and the profile was acquired (figure 3). The time dependence of the response is comparable to the current transformer diagnostics.

The Silicium carbide wire shows a very good resistance to deterioration and allows the observation of a 2 ms 95 mA 95 keV pulse at 1 Hz repetition rate.

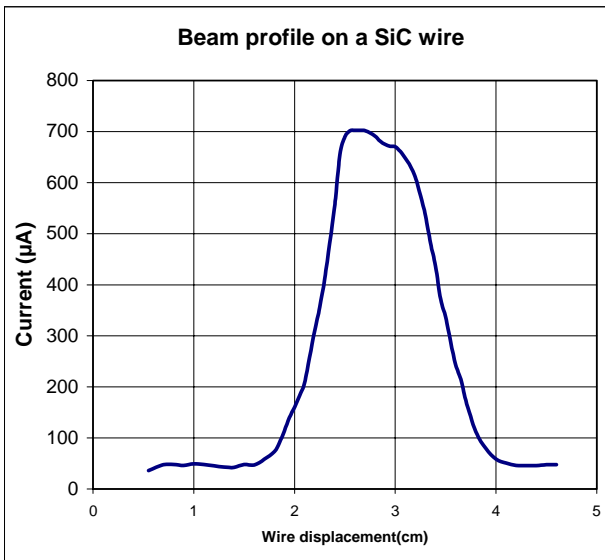


Figure 3 : Measured beam profile
on a 85 mA – 95 keV beam

TASK LEADER

Robin FERDINAND

DSM/DAPNIA/SACM
CEA-Saclay
F-91191 Gif-sur-Yvette Cedex

Tél. : 33 1 69 08 96 91

Fax : 33 1 69 08 14 30

E-mail : rferdinand@cea.fr

REFERENCES

- [1] P-Y. Beauvais, "Status report on the construction of the French high intensity proton injector (IPHI)", proceeding of EPAC 2002, Paris, page 539-541.

REPORTS AND PUBLICATIONS

CEA-DSM-DAPNIA-SACM contribution to the IFMIF KEP phase June 2000 to December 2002, Ref DSM/DAPNIA 03-72.

R. Gobin et al., "Status of the light ion source developments at CEA/Saclay", Rev. Sci. Instrum. to be published, oral presentation at the ICIS 03 conference (Dubna, Russia).

CEA-DSM-DAPNIA-SACM contribution to the IFMIF transition phase 2003, Ref DSM/DAPNIA 04-35.

Task Title: IFMIF, ACCELERATOR FACILITY
Analysis of possible alternatives developed in the Key Element
technology Phase (KEP), to the reference design of accelerator system

INTRODUCTION

INTRODUCTION AND BACKGROUND

The task was completed in the framework of the CEA program on high-power particle accelerators supported by the IPHI demonstrator project [1]. This project is dedicated to high power beam production (CW beam, 100 mA).

Other possibilities seem to arise to challenge the reference design in terms of accelerator solutions and engineering. Work done in other MW projects may suggest and new engineering solution to dedicated problems. The main criterion to estimate the added value is the loss level compared to the reference design one. The IPHI Radio Frequency Quadrupole (RFQ) under construction shows some delicate points needed to be followed. Alternative 4-vanes concept needed to be evaluated in terms of feasibility for the IFMIF project. An alternative profile for the electrodes was tested. Other RFQ design was tested.

CAVITY TYPES

One of our actions was to identify the different RFQ types available. We were helped in this task by Romuald Duperrier who made such a comparison for the RIA project at MSU [2]. This project is at 80 MHz, about 2 times a lower frequency than the IFMIF project.

Nevertheless the results are fully relevant for the IFMIF RFQ. One has to remember that 80 MHz is much easier to build from the engineering point of view.

A comparison of the power consumption of the most common RFQ structures was made: split coaxial, four rods, IH, and four vanes. The quality factor and peak power densities were computed and compared whenever possible with some experimental case (3D extremity of the IPHI RFQ).

In all the above RFQ cases the hypotheses were kept constant (same aperture, same vane voltage, same frequency). It is exactly the same accelerating structure.

Split coaxial

The split coaxial is a kind of 4-vanes RFQ with coupling cell between the vanes. It is a low power consuming cavity type. This property allows high voltage and big apertures (1 cm) especially at low frequencies and might be relevant for heavy ions when four vanes RFQ could be estimated too bulky. The main advantages of conventional Split Coaxial RFQ resonators are:

- High shunt impedance.
- Good tuning possibilities.
- No dipolar component.
- High mechanical stability.

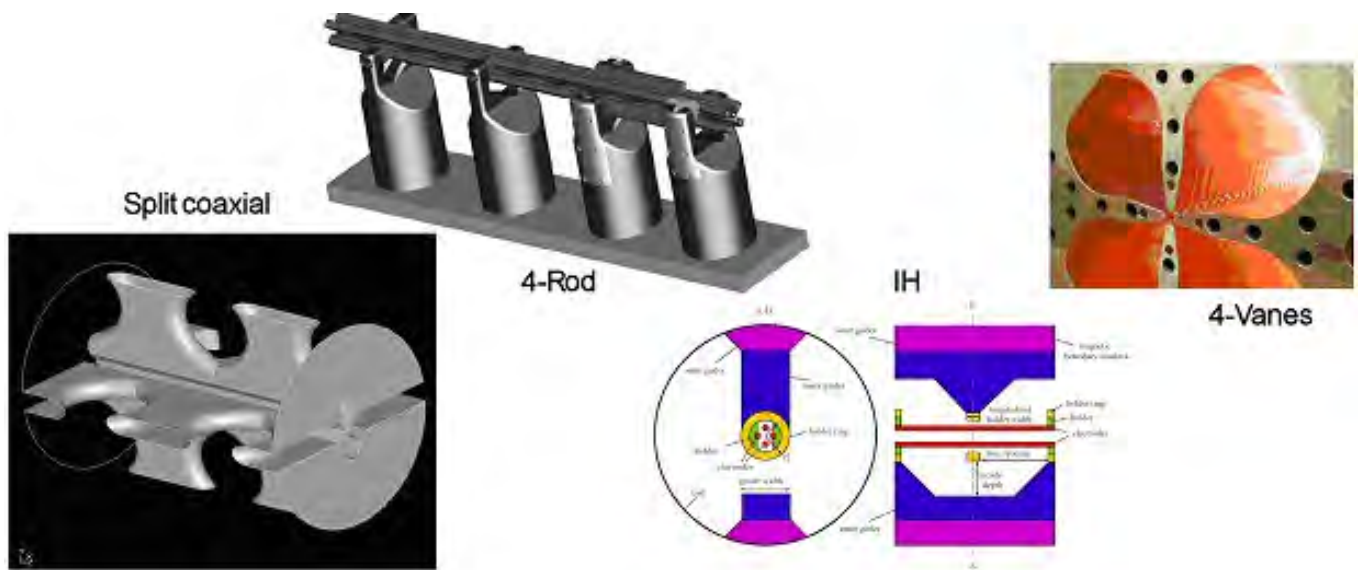


Figure 1 : The cavity types evaluated for the comparison

In table 1, the structure was not completely optimized. Usually, we try to minimize the transverse size by using this type of cavity.

Doing so, the coupling windows increase in size and the power dissipation (and peak power) increases. Nevertheless, the order of magnitude is more than sufficient to take a decision.

Four-rod

Four rods RFQ accelerators are well established and are the most common structure for the acceleration of heavy ions, generally in pulse mode. This 4-Rod RFQ was optimized by Holger J. Podlech for the same RIA project [3]. Among the advantages of 4-Rod RFQs, one can quote:

- Low cost.
- Suitable for heavy ions accelerator.
- Strong European team.
- Small transverse size.

IH RFQ

The IH was again optimized by Holger J. Podlech for the RIA project [3]. IH RFQs are relatively new developments. The first IH RFQ has been commissioned successfully in 1999 at GSI. The resonant structure consists of two girders carrying the support rings and mini-vane like electrodes (see figure 1).

Due to the small distance between the support rings (~10 cm), the losses around the electrodes are very small compared to four rods RFQ. This reduces the cooling requirements in this area. The main advantages of IH RFQ resonators are:

- Good shunt impedance and excellent distribution of losses.
- Good tuning possibilities.
- High field symmetry.
- High mechanical stability.

Four-vane

The 4-Vane structure is the eldest one and the most built for RFQs. It has been used for CW operation at 80 MHz [4] and at 350 MHz successfully [5,6]. It is the reference design. 4-vanes RFQs are well known in the laboratory [1].

They have shown good reliability in CW condition [7]. The main disadvantage is that the inductance is only 2D. This induces huge transverse cavities at low frequency. Due to the perfect quadrupolar symmetry, no dipolar component is present in the four vanes cavity. It is the most stable cavity type among the 4 presented, and allows the best field tuning.

In order to show a fair comparison, the following table also shows the 3D extremity of this essentially 2D accelerator (where the peak power loss is located).

Results

Table 1 : Comparison between RFQ structures

	Split Coaxial	Four rods	IH	Four vanes
Q	13985	6311	9362	17901/12819
E ₀ (MV/M)	17.73	20.00	19.34	17.41
B ₀ (T)	0.0048	0.0340	0.0126	0.0074
Power loss (kW)	49.2	80.4	77.8	37.46
Peak power loss (W/cm ²)	1.75	91.48	10.71	4.34

This table generates a few comments :

- Four vanes structures are the less consuming structures (more than a factor 2 compared to 4-rods or IH).
- Four rods RFQs show a very high peak power loss. The value can be manageable (we deal with higher peak value in the IPHI RFQ), but induces engineering difficulties and possible deformation in CW mode. This promises to be even more problematic at the IFMIF frequency of 176 MHz.
- Split coaxial RFQs looks not far from 4-vanes RFQs.

Taking these results into account, we do not recommend to change from the 4-vane RFQ type.

REVISIONS AND VERIFICATION OF THE RFQ BEAM DYNAMICS DESIGN.

RFQ Design comparisons

We looked at the different RFQ design of the IFMIF RFQ. The comparison extended to various RFQ codes, with the help of Dr. R. Jameson that we thank here. The first RFQ design was made in June 2002 by CEA-Saclay, and is documented in the previous report. The second one was provided during the same period by the Frankfurt team. Both designs showed a length of about 12.5 m, and cannot be compared on that point.

Table 2 : Comparison of the 2 RFQ design

	Saclay	FZK
Length (m)	12.482	12.211
Kilpatrick	1.76 at cell 8	1.64 at cell 656
Max vane voltage (kV)	130	152
Min vane voltage (kV)	96.5	67
Mean voltage (kV)	102.7	100.7
TOUTATIS Transmission (%)	98.4	97.12

Code comparison

There was a question on the results of the different RFQ simulation codes. We already know from a previous analyses that [8]:

PARMTEQM is not good for particles coming too close to the vane, as it is usually the case with high intensity beam. Above the circle defined by the minimum vane aperture, the fields are not well describes (10 % error on some surface, 100 % error on some spots). Depending on the PARMTEQM version, the particles might be considered lost above the square defined by the minimum vane aperture. This may lead to more losses (around 4.4 %) on some design. Some paraxiality was left in the PARMTEQM code, even when it was sure that it has been removed (found in the movement integration, $V_{tot} = Vz$).

Some comparison was made between PARMTEQM with and without paraxiality and TOUTATIS, with the assumption that a particle is lost on a square (like in PARMTEQM). The following table showed the results obtained at that time [8]:

	Transmission
TOUTATIS with the square	92.45 %
PARMTEQM with some paraxiality	87.22 %
PARTEQM without paraxiality	92.48 %

These results depend on the confinement level of each design and may vary, but the tendency is described.

Some precisions:

TOUTATIS can use a vane profile input file which describes both the longitudinal and the transverse shape of each four vanes (or rods). Since TOUTATIS calculates the 3D fields in real time, it can simulate all type of vanes defects, and naturally includes multipoles, images effects etc...

The space charge routine is a symplectic 3D routine.

The assumptions in the simulations were:

- Input emittance = 0.25π .mm.mrad rms normalised, 4D waterbag distribution leading to 1.5π .mm.mrad total normalised emittance.
- Input current such that 125 mA are accelerated out of the RFQ. In CEA-Saclay design this leads to 130 mA, input beam.
- No coupling gaps, since the exact number of coupling gaps was not yet fixed at the time of the comparison
- Sinusoidal z profile, $\rho \neq \text{const.}$, $\rho/R_0 \neq \text{const.}$

TOUTATIS results on the Saclay design revealed that one can expect up to 98.4 % of transmission, in real 3D field.

The output transverse emittance is equal to 0.28π .mm.mrad. With the 2-term formulation activated 99.5 % (no image effects) was obtained, so the 2 terms option in PARMTEQM could not explain a lower transmission. With the 2-term options and the “lost on square” option activated in TOUTATIS, we were very close to the PARMTEQM code. 95 % of transmission was observed. At 0 current there are no losses.

TOUTATIS results on the Frankfurt design with the same input beam the transmission was 97.12 %. The output transverse emittance is also equal to 0.28π .mm.mrad.

PARMTEQM simulations with multipoles, square criteria and some paraxiality gave 83 % transmission. With a corrected version (with multipoles and square criteria) we obtained 90 %.

The Saclay design was tested with the LIDOS.RFQ code. We spent a lot of time to ensure that we were simulating the same 3D copper profile of the vane. Then, LIDOS.RFQ has a different way to calculate the 3D field and the transport (compared to TOUTATIS), but there is again much less approximation in both TOUTATIS and LIDOS compared to analytical codes. The input beam was a 4D WB distribution. The transmission was 98 % with 97.8 % of accelerated beam.

Conclusions

The 2 terms formulation run in TOUTATIS shows that we may have confidence in the external field calculations of the TOUTATIS code. PARMTEQM is pessimistic for beam simulations which are big compared to the aperture.

There is not much difference between the two RFQ design. The Saclay design shows a slightly higher transmission, and a lower peak vane voltage, but both arguments are weak.

REFLECTIONS ON THE RFQ 2D CAVITY

The optimization was greatly simplified with the use of the 2D code SUPERFISH. Compared to other 3D codes, results are extremely fast and reliable to obtain.

The objectives described in this section were to test some tricks able to reduce the transverse size of the RFQ. A smaller transverse size means less expensive copper volume and a lower machining process.

This analysis was made previously to the 2D shape optimization described in task D5. For this only reason some discrepancy appears in the 2D shape. Nevertheless the tendency is accurately calculated and do not change the conclusion.

SUPERFISH calculations showed that the peak power loss, in 2D, is expected to be located in the bottom of the RFQ (see figure 2). The SUPERFISH power consumption was found to be equal to 61 kW/m with only 90 kV on the vanes.



Figure 2 : 1/8 of RFQ

A tentative was made to compensate the magnetic length of the RFQ (the bottom cavity, where is located the peak power loss), with an increased capacity around the beam axes. As it is not allowed to modify the vane tips profile, the idea was to introduce an over-thickness that we name the crocodile effect.

The transverse dimension was easily reduced by 8 %, but this was at the cost of a much higher hot spot and power consumption. The peak power loss increases by 41 % and the total power by 35 %.

Knowing that the power consumption is already a difficult point of the project, since it leads to use more of the expensive diacode, we abandoned this idea.

REFERENCES

-
- [1] P-Y. Beauvais, "Status report on the construction of the French high intensity proton injector (IPHI)", proceeding of EPAC 2002, Paris, page 539-541.
 - [2] "Power consumption comparison between different RFQ structures in favour of the RIA project", Romuald Duperrier CEA-Saclay, Felix Marti NSCL, MSU note, November 2002, 12 pages.
 - [3] H. Podlech et al., "Electromagnetic design of an 80.5 MHz RFQ for the RIA driver linac", proceeding of the EPAC 2002, Paris, France, p. 942.
 - [4] W. D. Cornelius, "CW Operation of the FMIT RFQ Accelerator", p 3139, Proc. of the 1985 Particle Accelerator Conf.
 - [5] L. Young, "Segmented Resonant Coupled RFQ", proceeding PAC 1993, Washington, D.C.
 - [6] H. V. Smith Jr, J. D. Schneider and R. Sheffield, "Low-Energy Demonstration Accelerator (LEDA) Test Results and Plans", proceeding of PAC 2001, Chicago, page 3296-3298.

[7] J. D. Schneider, "A review of high beam current RFQ accelerator and Funnels", p.128, Proc. of the EPAC'98 Conference.

[8] Romuald Duperrier thesis, "Dynamique de faisceaux intenses dans les RFQs", université Paris sud Orsay, n° 6194, july 2000. Exist in English version.

REPORTS AND PUBLICATIONS

CEA-DSM-DAPNIA-SACM contribution to the IFMIF KEP phase June 2000 to December 2002, Ref DSM/DAPNIA 03-72.

CEA-DSM-DAPNIA-SACM contribution to the IFMIF transition phase 2003, Ref DSM/DAPNIA 04-35.

TASK LEADER

Robin FERDINAND

DSM/DAPNIA/SACM
CEA-Saclay
F-91191 Gif-sur-Yvette Cedex

Tél. : 33 1 69 08 96 91
Fax : 33 1 69 08 14 30

E-mail : rferdinand@cea.fr

Task Title: IFMIF, ACCELERATOR FACILITY Engineering design outline, High Energy Beam Transport (HEBT)

INTRODUCTION

INTRODUCTION AND BACKGROUND

The task was completed in the framework of the CEA program on high-power particle accelerators supported by the IPHI demonstrator project [1]. This project is dedicated to high power beam production (CW beam, 100 mA).

The radio frequency (RF) study of the cavity has been focused. Two and three-dimensional electrodynamics simulations of 175 MHz four vanes structures with SUPERFISH and SOPRANO code have been done. Extremities and coupling gaps were studied.

The high-energy beam transport part was simulated. Different schemes for the distribution of the two 125 mA beams on the window were studied, and a new error study, including the HEBT was made.

2D-CAVITY

IFMIF RFQ quadrupole mode resonant frequency has to be 175 MHz which is roughly IPHI half-frequency [1]. An easy way of doing would be to simply double the main sizes. Instead, an attempt was made to still decrease the power losses.

Moreover, it was chosen to make the flat bottom wide enough (> 80 mm) to allow the insertion of appropriate slug tuners and vacuum port anywhere along the RFQ. In order to still decrease RF power losses, the vane thickness was reduced to 12.5 mm. The cell 151 defined the cavity volume and SUPERFISH program was run looking for optima as regards power consumption and flat bottom width.

A special program interacting with SUPERFISH was written to fit the value of the bottom to the accurate resonant frequency taking into account the same constraints as for cell n°151. Each cells were so optimized.

The integration of the 2D-power dissipation along the RFQ then gave the optimized whole 2D-power consumption, on top of which 20 % was added in order to take into account global 3D effects. This leads to $P = 654$ kW, about half of the power consumption expected.

Adding globally 50 % for the tuning, RF transport losses and adding the beam power we obtain a total of 1591 kW allowing the use of **only two** RF systems instead of the three previously anticipated.

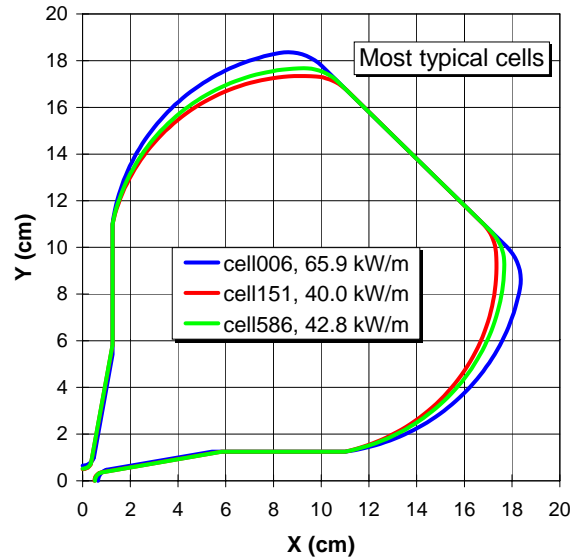


Figure 1 : Optimized cross-section of IFMIF RFQ most typical cells

IFMIF RFQ COUPLING GAPS

Resonant coupling segmented RFQ were first introduced by Lloyd Young from Los Alamos National Laboratory. Resonant coupling in a segmented RFQ stabilizes the accelerating field against quadrupole-like perturbations. End rods are also used to stabilize the field against dipole-like perturbations. As a result, the distribution of nearby modes about the accelerating mode frequency is optimized.

Extensive analytical developments in Saclay now allow to calculate the effects of the segmentation on the RFQ quadrupolar component stability. We check the need of coupling segments and calculated the according gap width.

The stability quality of the quadrupolar factor was evaluated as a function of the longitudinal capacitance in the segmentation.

A minimum is observed for 3 segments, with a coupling capacitance of about 2 pf. 1 segment would even work, but with less possibilities for the dipolar finger insertions. We recommend that the IFMIF RFQ be cut in three resonantly coupled segments. In such a case, the beam dynamics indicates that they will be located at 4.161 and 8.321 meter.

The numerical calculation of the gap capacitance versus the gap properties was made with the Vector Field code TOSCA[®]. The gap width for a 2 pf capacitance is equal to 2.32 mm.

THE IFMIF HIGH ENERGY BEAM TRANSPORT

General description

The incidence angle of each beam at the target is obtained with one achromat composed with two 4.5° bend. This allows for a cost reduction when compared to the previous design [2] and an operation simplification. The achromat is located near the accelerating system output. At this location, the energy spread growth induced by the space charge is minimized. The line length after the deviation is set in order to reach the horizontal separation between the target center and the linac reference line. The present design is 5.3 m long, and this can be insufficient, but the lengthening of the last drift can increase this distance. The total line length is 43.12 m. Transverse uniform shape is obtained using non-linear multipole lenses (octupoles and duodecapoles).

The line is divided in three functional sections:

The goal of the first section, which includes the achromat, is to match the linac output beam through the achromat and for the entry in the second section.

In the second section, the optical conditions are designed in order to allow for insertion of the octupole and duodecapole lenses at 4 positions.

The last section, including the beam expansion drift, allows the matching of the needed footprint sizes at the target.

This organization allows an easy operation of the line tuning. All the first order simulations are performed with the code BETA. The tuning of the octupoles [3,4] assume hypothesis. The transverse motions are supposed to be fully uncoupled (the space charge coupling is assumed negligible). The non-linear lenses dedicated to the horizontal distribution flatness (and respectively the vertical distribution) are supposed to be located at a waist of the vertical motion (respectively the horizontal). When the beam sizes, at the multipole location, are small in one plane and large in the other one, the multipole have an effect in the plane where the beam is sufficiently big. Four positions, where the beam sizes have the previous properties, are achieved with 6 quadrupoles. This allows for the insertion of 4 multipoles, 2 for each plane. The 2 duodecapoles role is to improve the beam flatness by folding back the tails created by the octupoles.

The last section has to match the target footprint beam sizes to the requirements. This is made with 6 quadrupoles.

PIC simulations transport and losses

A 1,000,000 macroparticles 4D water-bag distribution is used at the input of the RFQ. The transverse rms normalized emittances used are $0.25 \pi \cdot \text{mm} \cdot \text{mrad}$. The beam current is 130 mA. Multiparticle simulations are then done from the RFQ output in the full Drift Tube Linac (DTL). And finally, the output DTL beam distribution is injected in the HEBT line. The beam footprint are plotted below.

Ele: 855 [88.6514 m] NG00D : 1082613 / 1082613 TraceWin - CEA/DSM/DAPNIA/SACM

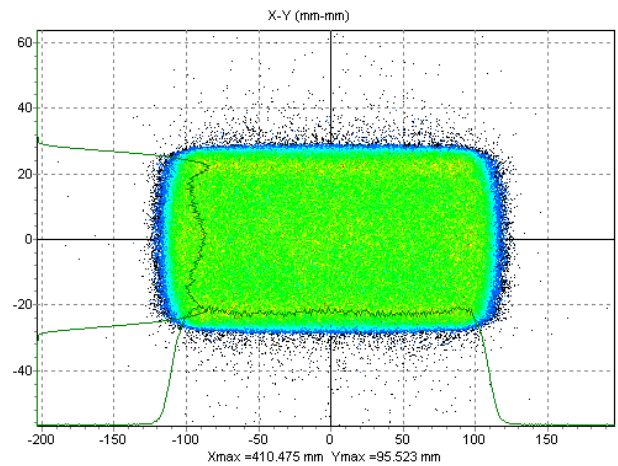


Figure 2 : Output HEBT beam distribution

These results indicate that the deviations from uniformity in the flat-top region are in the range of $\pm 7\%$, rather than the desired $\pm 5\%$ in vertical plan while the horizontal beam distribution fill up better than the requirements. The peaks along the horizontal edge rise are much better than the desired 15% . But the $0.5 \mu\text{A}/\text{cm}^2$ beam density beyond 22 cm are clearly out of reach, especially in a space-charge regime.

The simulation using the beam distribution from the DTL shows losses mainly located in the non-linear lenses, where the pipe radius is the smallest (5 cm). About 44 macroparticles over 1,000,000 are lost. They correspond to about $6 \mu\text{A}$ and 240 W. The same simulation performed with an initial 4σ gaussian distribution shows **no loss**. A possible way to avoid losses all along the HEBT and minimize activation of the accelerator components is to reduce beam halo with a scraper. A dedicated scraper can be designed to support more easily the losses and allow easier shielding than multipole elements. The simulation shows no loss if it is located after the achromat line. The removed beam portion corresponds to 0.02% (1 to 2 kW). The scraper avoids the losses in the multipole lenses.

Sensitivity to linac element errors

Two families of errors may occur:

Static errors: the effect of these errors can be detected and cured with appropriate diagnostics and correctors. Correction strategy should be known to be able to estimate their impact on beam dynamics.

Dynamics errors: the effect of these errors is assumed to be uncorrected. Fortunately, they have usually lower amplitude than static errors. There are, for example, the vibrations or the RF field variations.

Quadrupoles may have a wrong position, be tilted, or have a wrong gradient. Cavities may have a wrong position, be tilted, or have a wrong field (phase and/or amplitude). An unperfect beam position measurement has also to be taken into account.

There is no errors on the dipole elements in the present study. Errors with different amplitudes have been used depending on the linac section.

To correct beam misalignments in the DTL, couple of steerers are placed into the last tubes of each tank and a couple of BPM are placed between tanks. In the HEBT, 6 correction-set are necessary to control efficiency the beam central trajectory. The correction scheme is efficient in the DTL (lower than 1 mm) and is more difficult in the HEBT line, especially in the last 17 m drift which is very sensible.

At present time, we did not include in our simulation specific diagnostics to correct the gradient errors which cause mainly mismatching. Thus, we consider that the error studies results below show a worse beam behaviour than the normal operating mode where some specific diagnostics are used to match the beam to take into account the machine errors.

HEBT Error studies

We studied first the HEBT line alone. The transport of a 100,000 macroparticles beam has been simulated in a set of 110 different HEBT lines with all combined errors on each element. The total number of particles used is about 10 millions. The beam distribution from DTL has been used. We observe that 1200 W are dissipated in the scraper. For a pipe radius limited at 200 mm in the last expanded beam pipe, 1 particle over 10⁶ will be lost.

The distribution in figure 3 represents the superposition of 100 different simulated linacs with all the combined errors (about 10,000,000 particles). It's not the beam at the target, but the probability to reach this density at the target. We notice that the distribution is still close to the requirements. The imperfections mainly degrade the beam fringes and increase the beam noise.

ODD : 10810750 / 10810750 I=127.8 mA TraceWin - CEA/DSM/DAPNIA/SA

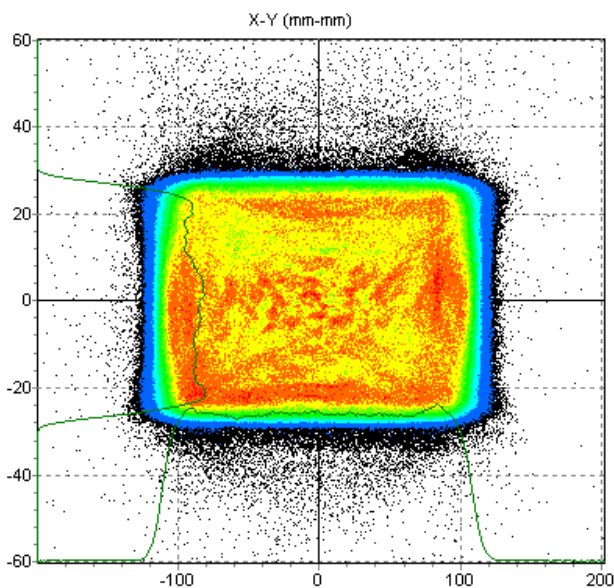


Figure 3 : Output HEBT beam distribution (HEBT error)

End-to-End errors study

The linac (RFQ-DTL) used in this study is the IFMIF reference design [5]. The transport of a 100,000 macroparticles beam has been simulated in a set of 110 different linacs with all combined errors on each element. The total number of particles used is about 10 millions. The simulation begins at the RFQ input. All the previously listed errors are used. The output distribution characteristics are close to the requirement expected 0.5 μA/cm² beam density beyond 22 cm.

the losses repartition along the structure and the corresponding dissipated power is 1.98 % in the RFQ, 0.18 % in the DTL and 0.17 % in the HEBT. Remember that no matching has been used to control the beam mismatching due to focalization errors, while it will be partially corrected in real operation.

The first end-to-end errors study made in 2002 didn't show any loss in the DTL [5]. Two reasons explain the today results: More errors have been taken into account like vibrations, phase and field errors, tanks displacements and vibrations, BPM errors... The statistic was 100 runs of 10,000 macro particles compared to the 100 runs of 100,000 macro particles of the present study. It didn't allow to observe loss intensity lower than 128 nA.

Several methods can be explored in order to reduce these losses:

Change the DTL design without increasing the number of diacode, in order to increase the aperture drift tube from 12.5 mm to 14 mm or more (using also 2 quadrupole length), the RFQ machining tolerance could be slightly decreased. Another method is simply to scale all the drift tube and quadrupole dimensions.

CONCLUSION

The tasks were completed on time, with extremely valuable results. The main points are:

A dedicated H₂⁺ has to be developed if the idea of using H₂⁺ is kept for the linac conditioning.

The RFQ 2D profile optimization lead to a diacode saving. Only 2 1 MW diacodes are now needed.

The HEBT has been designed and extensively analysed. The requirements cannot be completely obtained on some points, due to the space charge. full errors study was made, that we can describe as the "worse case". It appears that a scraper is highly recommended in the HEBT line. Some room was left for a wall shielding.

REFERENCES

- [1] P-Y. Beauvais, "Status report on the construction of the French high intensity proton injector (IPHI)", proceeding of EPAC 2002, Paris, page 539-541.
- [2] JAERI-Tech 2003-005, IFMIF-KEP, Key element technology phase report.
- [3] F. Meot, T. Aniel, Principles of the non-linear tuning of beam expander NIM A379 (1996).
- [4] F. Meot, T. Aniel, On beam uniformization by non-linear optics CEA/DSM/GECA/ 95-05, July 1995.
- [5] R. Duperrier, D. Uriot , N. Pichoff , R. Ferdinand "Beams dynamics end to end simulations in IFMIF Linac" EPAC 2002, Paris.

REPORTS AND PUBLICATIONS

CEA-DSM-DAPNIA-SACM contribution to the IFMIF KEP phase June 2000 to December 2002, Ref DSM/DAPNIA 03-72.

CEA-DSM-DAPNIA-SACM contribution to the IFMIF transition phase 2003, Ref DSM/DAPNIA 04-35.

TASK LEADER

Robin FERDINAND

DSM/DAPNIA/SACM
CEA-Saclay
F-91191 Gif-sur-Yvette Cedex

Tél. : 33 1 69 08 96 91

Fax : 33 1 69 08 14 30

E-mail : rferdinand@cea.fr

UT-TBM/MAT-LAM/DBTT

Task Title: INFLUENCE OF THE MARTENSITE MORPHOLOGY ON THE DBTT OF EUROFER STEEL

INTRODUCTION

Ferritic/martensitic steels such as EUROFER exhibit a Ductile Brittle Transition Temperature (DBTT). This temperature should be as low as possible to limit the risk of in service embrittlement. Various parameters have an influence upon the DBTT. For example, the precipitation of different phases within laths in the material can induce important an shift in the DBTT. For this reason, different studies have been performed to characterise the precipitation even at nanometric scale.

In this study, we will focus on another aspect of the microstructure that governs the DBTT : the lath packets size of the martensitic structure. The main objective of this task is to perform a generic study of the influence of this parameter on the DBTT of martensitic steels.

A better understanding of the parameters that influence the DBTT of martensitic steels will provide very useful information for prediction of this temperature.

2003 ACTIVITIES

2003 activities consisted of completion of the mechanical characterisation of EUROFER steel in different metallurgical conditions and analysis of the relationships between the martensite morphology and the mechanical properties.

MATERIAL AND MICROSTRUCTURE CHARACTERISATION

The material studied in this task is the reduced activation martensitic steel EUROFER. The chemical composition of this steel developed by Europeans involved in fusion programs is the following:

Fe	C	N	Cr	W	Mn	V	Ta	Si
bal.	0.117	0.0219	8.96	1.04	0.48	0.18	0.15	0.03

The as-received (AR) conditions are: normalisation at 980°C for 30 min and tempering at 760°C for 90 min.

This steel was also tested in other metallurgical conditions such as:

- 1) Normalisation at 1150°C for 30 min and tempering at 760°C for 90 min. The Prior Austenite Grain (PAG) size is 100 µm.

- 2) Normalisation at 1050°C at a controlled heat rate and tempering at 760°C for 90 min to obtain a heterogeneous PAG size. With this heat treatment we obtained a PAG with sizes ranging from 15 to 150 µm approximately.

The microstructure of a martensitic steel within a PAG is often described as followed (see figure 1):

- Adjacent laths with the same variant (same crystallographic orientation) form blocks.
- Adjacent blocks with the same habit plane form packets.
- PAG is composed of several packets.

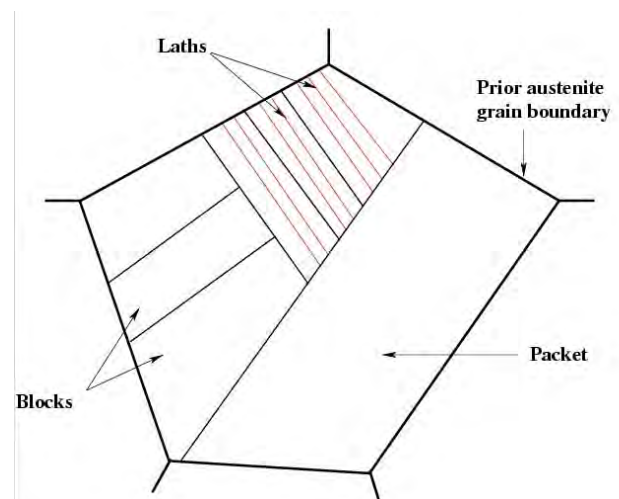


Figure 1 : Scheme of a PAG in a martensitic steel

If we consider that a block is formed by adjacent laths with a misorientation lower than 10°, then the block area can be deduced from EBSD (Electron BackScattering Diffraction) measurements in a SEM (see [1]).

In the framework of the action UT-TBM- LAM/MIC [1], we measured by EBSP the block area in Eurofer steel with various PAG sizes. In a 2 D section (metallographic observations or EBSD characterisations) the shape of blocks is more or less elongated.

We can simplify the description and consider that blocks are like grains in an equiaxed structure. The size “d” of an equivalent block was calculated by taking the block’s area average and by calculating d as a diameter of an equivalent disc.

With this approximation a relationship between the PAG size and the block size can be obtained (figure 2).

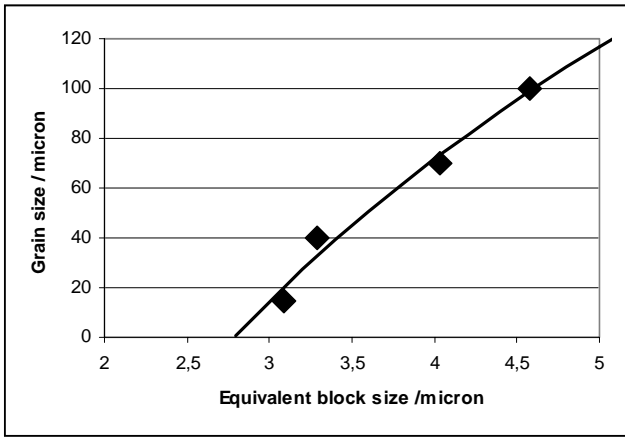


Figure 2 : Relationship between PAG size and block size in Eurofer steel (here a logarithmic relationship is plotted)

MECHANICAL PROPERTIES

Tensile properties

These were measured using cylindrical tensile specimens of 2 mm in diameter and 12 mm gauge length, machined parallel to the rolling direction (table 1).

Impact properties

Impact specimens were machined along the rolling direction. They were Charpy V-notch subsize specimens (KLST : 27 mm long, 4 mm wide and 3 mm thick).

The Ductile-Brittle Transition Temperature (DBTT), corresponding to 50 % ductile and 50 % cleavage fracture mode, was deduced from the half-value of the Upper Shelf Energy (USE) or from force-time curves (see table 2 and figure 3).

Table 1 : Tensile properties of EUROFER steel in different metallurgical conditions

	Test Temperature (°C)	0,2% Proof stress (Mpa)	U.T.S. (Mpa)
Eurofer AR (N&T) PAG : 15 µm	Room Temp.	526	666
	550	354	371
Eurofer N&T PAG : 100 µm	Room Temp.	550	680
	550	364	378

Table 2 : DBTT and USE of EUROFER steel in different metallurgical conditions

	DBTT (°C)	USE (J)
Eurofer AR (N&T) PAG : 15 µm	-100	8,3
Eurofer N&T PAG : 100 µm	-70	8,5
Eurofer N&T PAG heterogeneous : 15 to 100 µm	-105	8,3

INFLUENCE OF THE MARTENSITE MORPHOLOGY ON THE MECHANICAL PROPERTIES OF THE EUROFER STEEL

For normalised and tempered materials, after the tempering, the martensite structure can be considered as a set of ferrite laths decorated by a precipitation of carbides. In fact the misorientation between adjacent laths in the same block is low (a few degrees) and there is almost no precipitation of $M_{23}C_6$ carbides between adjacent lath with the same variant.

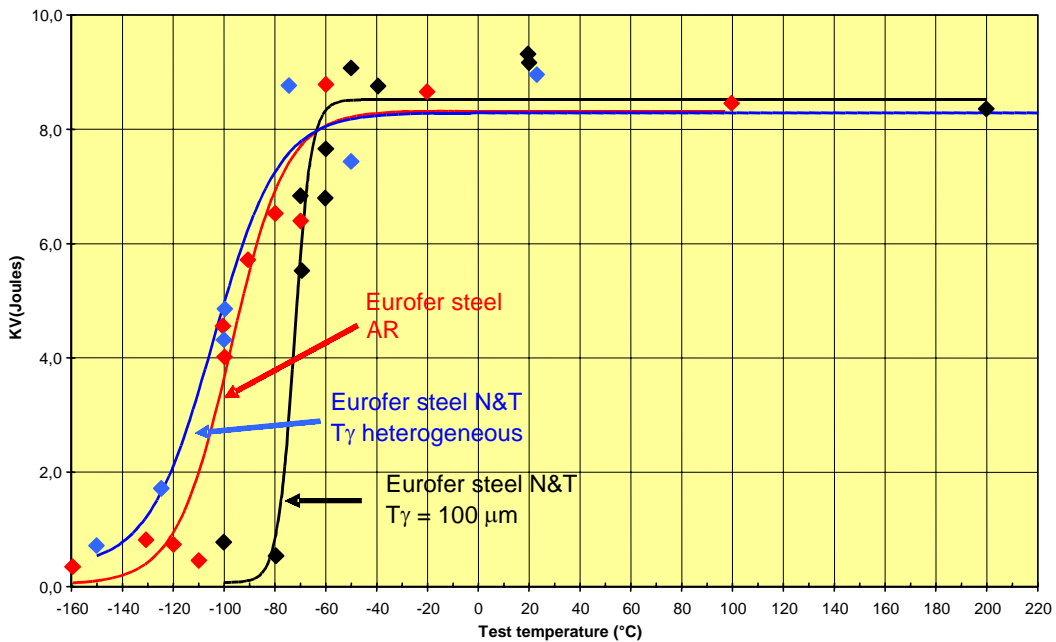


Figure 3 : Ductile/Brittle transition curves for the N&T Eurofer steels

An approximation to describe the microstructure consists in considering that the martensite structure is formed of an assemblage of ferrite blocks decorated by a precipitation of carbides. The typical size of blocks was deduced from EBSD measurements presented in figure 2.

Tensile properties

For normalised and tempered steels we could try to apply the normally called Hall-Petch law to describe the variation of the mechanical properties as a function of the block size. The Hall and Petch law is: $\tau_y = \tau_1 + k_y/d^{1/2}$

With τ_y is the proof stress, τ_1 the stress necessary to move the dislocations if the crystal were perfect, k_y is a constant which depends on the material and d the grain size.

If we consider that in martensitic steels (N&T), the characteristic dimension is in fact the block size, then the steel with the largest block size should exhibit the lowest tensile strength. Experimentally we do not observe this phenomenon (see table 1); the proof stress increased slightly with increasing the grain size. The homogenisation at high temperature (1150°C) of the Eurofer steel with the largest PAG probably induces a better dissolution of vanadium and/or tantalum carbonitrides. These can precipitate as fine particles in the matrix during the tempering process and increase the proof stress of the material. This phenomenon has already been observed in the Fe-9Cr1Mo modified steel [2]. This could explain why the N&T Eurofer steel does not follow the Hall-Petch law.

Impact properties

For BCC materials the DBTT is strongly affected by the grain size. A logarithmic relationship between the grain size d and the DBTT is often considered [3,4]:

$$DBTT = F + G \ln(d^{1/2})$$

where F and G are constants and d is the grain size. If we assume that the same relationship could be applied to the Eurofer steel by using the block size (calculated in the paragraph 2) as the grain size in this formula, then we are able to describe the variation of the DBTT as a function of the block size.

In figure 4, the black points are the experimental data and the dashed line is an extrapolation assuming the equation: $DBTT = F + G \ln(d^{1/2})$ can be applied. Experimentally it is not possible to increase the block size greatly to test whether this equation can predict the DBTT for larger block sizes; but we could obtain a ferritic structure by appropriate heat treatment. In that case the "block size" would be the grain size. According to figure 5, Eurofer steel with a ferritic structure and a grain size close to 15 μm should exhibit a DBTT around 0°C. This value looks reasonable according what we know on ferritic steels but it should be checked with other experiments. It is noticeable that the Eurofer steel (N&T) with an heterogeneous grain size has almost the same impact properties as the Eurofer (N&T) with a PAG close to 15 μm . It appears, the presence of only a few large PAG does not influence the impact properties.

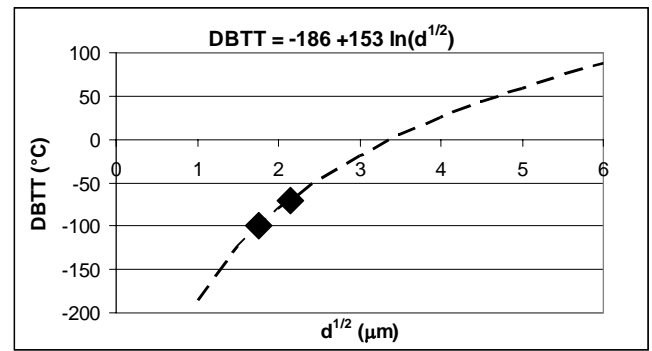


Figure 4 : Influence of the block size on the DBTT for Eurofer steel

CONCLUSION

The objective of this study was to try to correlate the block size of the Eurofer steel with its mechanical properties. For this purpose, measurements were made of tensile and impact properties of Eurofer steel in different metallurgical conditions and with different Prior Austenite Grain sizes. Microstructural characterisation by EBSD (Electron BackScattering Diffraction) in a SEM has previously been carried out [1].

From this characterisation and with some simple assumptions, we described the microstructure of the martensitic steels (N&T) as an assemblage of ferrite blocks decorated by a precipitation of carbides. Each block is formed by adjacent laths with the same variant, and can be interpreted as the equivalent grain for martensitic microstructure. EBSD measurements have shown that the block size increases slightly for PAG size from 15 to 100 μm . We tried to link the proof stress of N&T Eurofer steel with the block size using the Hall-Petch law.

The heat treatment apply to vary the block size probably induces a slight hardening of the matrix, and the Hall-Petch law is not followed. However, the usual relationship between the grain size and the DBTT for ferritic steel could explain the small shift we observed in the DBTT between the Eurofer with a PAG size of 15 μm and 100 μm . In this case, the characteristic structural unit of the microstructure which controls the DBTT would be the block size.

REFERENCES

- [1] F. Barcelo, "Caractérisation de la microstructure de l'acier martensitique EUROFER par EBSD ; influence de la taille de l'ancien grain austénitique", NT SRMA 2003-2525, Rapport Technologie Fusion UT-TBM/MAT-LAM/Mic.
- [2] J-C. Brachet, "Alliages martensitiques 9Cr-1Mo : effets de l'addition de l'azote, du niobium et du vanadium sur la microstructure, les transformations de phase et les propriétés mécaniques", thèse de doctorat, Université de Paris Sud centre d'Orsay, Juin 1991.

- [3] R.N. Wright, "Toughness of Ferritic Stainless Steels", ASTM STP 706, R. A. Lula, Ed., 1980, pp. 2-33.
- [4] D. François, A. Pineau, A. Zaoui, "Comportement mécanique des matériaux, viscoplasticité, endommagement, mécanique de la rupture, mécanique du contact", Hermès Ed., Paris 1993, 1995.

REPORTS AND PUBLICATIONS

Y. de CARLAN, "Influence of the martensite morphology on the DBTT of the EUROFER steel", NT SRMA 2004-2616, Rapport Technologie Fusion UT-TBM/MAT-LAM/DBTT.

TASK LEADER

Yann de CARLAN

DEN/DMN/SRMA
CEA-Saclay
F-91191 Gif-sur-Yvette Cedex

Tél. : 33 1 69 08 61 75
Fax : 33 1 69 08 71 30

E-mail : yann.decarlan@cea.fr

Task Title: PREDICTION OF THE DBTT OF MARTENSITIC STEELS BY NEURAL NETWORKS

INTRODUCTION

DUCTILE-BRITTLE TRANSFORMATIONS

Ferritic and martensitic steels undergo a transition from ductile to brittle fracture behaviour as the temperature is lowered. In order to reduce the risk of in-service embrittlement, the ductile-brittle transformation temperature (DBTT) must be minimised. An understanding of the effects of composition, heat treatment and other variables on the DBTT is therefore necessary.

A wealth of Charpy impact test data has been gathered over many years in our laboratory (SRMA). The aim of this study is to benefit from this large data set by subjecting it to a statistical modelling procedure which will then be able to make predictions based on the trends found.

NEURAL NETWORKS

Artificial neural networks are a tool to determine relationships and make predictions in situations in which physical models either do not exist or are too simple to take account of the influences of all the relevant variables and their interactions [1]. In the current context, for example, it is well known that the impact energy K_v depends on test temperature, but it is also affected to a greater or lesser extent by the alloy composition, heat treatment, specimen geometry and pre-test deformation. An empirical model able to take account of these parameters, and to make predictions, would be very useful in this situation.

Neural networks are a form of nonlinear regression analysis. In linear regression, the output y is calculated by multiplying each input x_j by a weight w_j , summing over all the inputs j , and adding a constant term θ (Equation 1). The disadvantage of this is that it assumes a linear relationship, which holds true throughout input space, between the inputs and output, which may not be the case in practice. The neural network method instead uses a flexible nonlinear function f , often the hyperbolic tangent, \tanh , for fitting. Further flexibility is provided by using several \tanh functions h_i , known as 'hidden units' in neural network terminology, which combine linearly to give y (Equation 2).

$$y = \sum_j w_j x_j + \theta \quad \text{Equation 1}$$

$$h_i = \tanh \left\{ \sum_j w_{ij}^{(1)} x_j + \theta_i^{(1)} \right\} \quad \text{Equation 2}$$

$$y = \sum_i w_i^{(2)} h_i + \theta^{(2)}$$

2003 ACTIVITIES

MODEL DEVELOPMENT PROCEDURE

The model was created with the aid of a piece of software called 'Models Manager' [2], which provides a user interface for the neural network model creation program written by MacKay [3] and associated database treatment utilities.

The development the neural network model took place in the following stages:

Selection of inputs and collection of data: A large database is needed if the model is to give good predictions. The experimental data used here are from Charpy impact tests on specimens of 9Cr steels with the "SRMA" specimen geometry. Included in the database are information on the steel compositions, heat treatments and test conditions. Figure 1 shows the ranges of the input parameter values present in the database. The neural network method also allows non-numerical parameters to be included by assigning them a numerical value. In this case, the orientations LT and TL are labelled as 1 and 2 respectively. This allows the effect of these parameters on the output to be determined in the same way as if they were simply numerical inputs.

The neural network program used to create this model includes an automatic relevance detection function allowing the significance of each input on the output to be quantified. As a result, there is no need to make any prior decisions about which inputs are relevant. Instead, all inputs for which complete and reliable data are available can be included.

Several datasets included more than one chemical analysis on the same sample; in this case, only the most complete analysis was included. Where no value was provided for the concentration of a certain element, a value of zero was substituted. This is a more reasonable solution in the case of elements deliberately added, such as W and Mo, than in the case of impurity elements such as S or P which are almost always present to some extent even if they are not quantified. It is intended to construct another model, in which the impurities are not included, for comparison with this first attempt at modelling. All data lines which were incomplete in any other way were deleted from the database.

Training This stage consists of optimising the coefficients $w_{ij}^{(1)}, w_i^{(2)}, \theta_i^{(1)}$ and $\theta^{(2)}$ in Equation 2, and the number of hidden units, to give a model which both fits well to the data supplied to it, and generalises to make reasonable predictions.

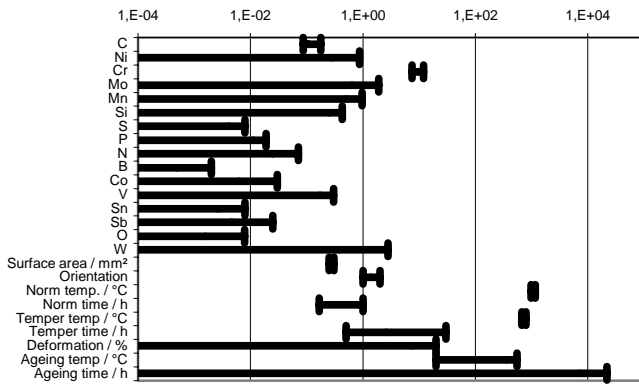


Figure 1 : Ranges of input values in database - All compositions are in wt. %

One potential problem with a model consisting of a large number of flexible functions is that it is able to fit noise in the data as well as the true trends ('overfitting') resulting in poor generalisation.

Two methods are used to avoid this. Firstly, only half the data set is used for the training; the other half is set aside for testing.

The Models Manager program performs the sorting and dividing process. Secondly, the error function minimised during training consists of two terms: one characterises the difference between real data and predictions, and the other favours simpler over more complex models.

In practice, around 100 models, with different numbers of hidden units and different seed values (starting points for minimisation) are trained.

In the current model, the maximum allowable number of hidden units was set to 20, the default setting suggested by Models Manager. The trained models were compared with the test data set and ranked.

Forming a committee In regions where the data are sparse or noisy, several possible models may fit the surrounding regions adequately and give a reasonable interpolation in the sparse area. It has been found that if the best N models, as ranked by log predictive error, are combined and the prediction obtained as the average between them, then a better fit to experimental data is obtained than by using the best single model.

The value of N chosen is that which gives a minimum error when tested against experimental data. For this first model, it was decided to use the value $N=20$ suggested by Models Manager.

TEST OF NEURAL NETWORK MODEL PREDICTION

The Models Manager software includes a 'predictor' module which enables the user to enter a set of compositional and experimental conditions and obtain a prediction of the variation of the property of interest with respect to one of the inputs.

In order to test the quality of predictions, typical composition and heat treatment values for a modified 9Cr1Mo steel were entered and a prediction of the variation of K_v with test temperature was made.

Figure 2 shows this neural network prediction as a solid line, together with experimental points for this steel. Typically, a hyperbolic tangent function is fitted to experimental K_v values, applying the condition that the fitted curve should not fall below $K_v = 0$.

Such a condition cannot easily be applied to the neural network algorithm, with the result that sub-zero predictions are observed in Figure 2 outside the temperature range of the experimental data. With sufficient numbers of low-temperature data, it may be possible to train a neural network model not to predict values below zero, since the model bases its predictions upon the data provided to it.

The size of the error bars, calculated by the neural network program, is a measure of the uncertainty in the prediction, and is greatest in regions in which the data are sparse or noisy. In figure 2, the error bars remain approximately constant throughout the temperature range considered, because data sets included in the database were obtained at evenly spaced intervals of test temperature. Given the close agreement between model and experiment observed here, it appears that the error bars are overly pessimistic in their assessment of the predictive ability in this case.

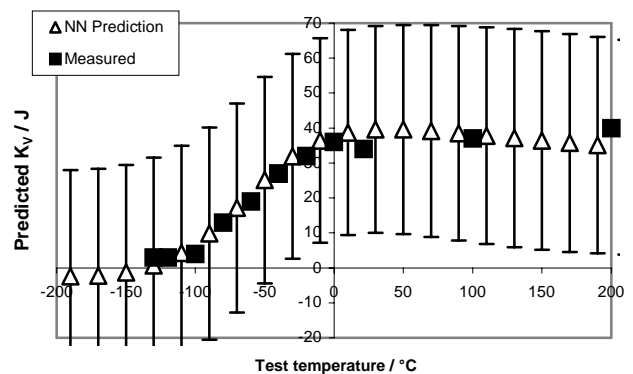


Figure 2 : Neural network prediction and experimental measurements of K_v for modified 9Cr1Mo steel

CONCLUSIONS AND FURTHER WORK

A piece of software, "Models Manager", enabling the creation of neural network models, has been acquired by our laboratory (SRMA) and used to make a first attempt at modelling the dependence of K_v on composition, thermomechanical treatment and test conditions. The model shows good agreement with experiment when tested on a modified 9Cr1Mo steel. Subsequent work will test whether it is better to include or exclude the incomplete impurity data. The best solution may be to train one model on the subset of complete impurity data, and another on the whole of the current dataset without the impurity data. In this way, both a general model and a model of the effect of impurities could be obtained.

The database can then be augmented with data from the latest tests on reduced activation steels (Eurofer, JLF-1, F82H), both from CEA laboratories and from the literature, to improve the predictive capacities of the model. Finally, the work can be extended to irradiated material to give predictions of irradiation effects on DBTT.

REFERENCES

- [1] Bhadeshia, H. K. D. H., ISIJ International, 39, 1999, 966-979.
- [2] http://www.msm.cam.ac.uk/phase-trans/2001/mm_doc/index.html
- [3] MacKay, D. J. C., 'Bayesian Methods for Adaptive Models', PhD thesis, Caltech, 1992.

REPORT

Yardley, V. A., 'Prediction of the DBTT of martensitic steels by Neural Networks', NT SRMA, to appear shortly

TASK LEADER

Yann de CARLAN

DEN/DMN/SRMA
CEA-Saclay
F-91191 Gif-sur-Yvette Cedex

Tél. : 33 1 69 08 61 75
Fax : 33 1 69 08 71 30

E-mail : yann.decarlan@cea.fr

Task Title: DEVELOPMENT OF NEW RAFM STEELS WITH REGARD TO CREEP PROPERTIES

INTRODUCTION

Martensitic 8-12Cr steels are under development as candidate materials for fusion reactor components because of their excellent dimensional stability under irradiation. These materials are based on Fe 9/12Cr steels and contain tungsten and MX-carbonitride formers such as vanadium or tantalum. In order to reduce the radiological impact of these materials, certain alloying additions, for example Mo and Nb, must be forbidden.

A review of the literature on 8-12Cr steels suggested several routes for the improvement of creep properties, including optimisation of the content of solid solution strengthening elements in the matrix, reduction of the nickel, silicon and manganese contents, and promotion of the precipitation of a fine distribution of MX carbonitrides, such as vanadium nitride (VN) or titanium carbide (TiC), which help to stabilise the dislocation network [1]. It was decided to design both VN- and TiC-strengthened alloys.

Thermodynamic modelling tools were used to determine the composition ranges for which the MX particles could be put into solution without risking the formation of δ -ferrite, which is an undesirable phase because of its brittleness. For the VN-strengthened compositions, a neural network model was also used to select the composition which gave the maximum creep rupture strength after 1×10^5 hours at 650°C. (This procedure could not be carried out for the TiC-strengthened steel because Ti is not included in the neural network model.) The compositions chosen for fabrication, V1, V2 and Ti1, are listed in table 1.

Table 1 : Compositions of designed alloys V1, V2 and Ti1, in wt. %

	C	N	Cr	W	V	Ti
V1	0.1	0.085	9	1.5	0.32	
V2	0.1	0.07	8	2.5	0.35	
Ti1	0.05		8	1		0.2

2003 ACTIVITIES

FABRICATION OF THE EXPERIMENTAL ALLOYS V1, V2 AND TI1

Small ingots of the three compositions listed in table 1 were fabricated by Aubert et Duval using the Vacuum Induction Melting (VIM) technique. The composition of the fabricated product was in good agreement with the specification.

Macrographic examination of the solidified ingots of the two VN-reinforced steels revealed the presence of circular pores of diameter ~ 10 mm. The shape of these defects suggests that they originate from bubbles of nitrogen gas. Attempts to close the defects by forging having been unsuccessful, a change in composition must be considered for the further development of these materials. However, the macrograph of the Ti1 casting did not show any defects. Ultrasonic testing on Ti1 revealed the presence of 'indications' which, on metallographic examination, were found to be clusters of oxide inclusions trapped in the metal during fabrication. These are extrinsic defects which can be removed by remelting. The Ti1 steel can therefore be regarded as having been successfully fabricated, and work can go ahead on developing this material.

PHASE STABILITY CALCULATIONS ON VN-REINFORCED ALLOYS

9Cr steels with nitrogen contents of around 700 ppm have already been fabricated without any similar phenomenon being observed, so it appears that it is due to a more complex set of circumstances than simply an excess of nitrogen.

In order to try to understand and remedy the problem, phase stability calculations were carried out using the thermodynamic calculation software 'ThermoCalc', both on the alloys V1 and V2 and on other alloys in which porosity was not observed. Although ThermoCalc only calculates phase stabilities at equilibrium, it was hoped nonetheless that it would provide insight into the compositional conditions favouring gas evolution.

Initial stepped calculations demonstrated that gas was an equilibrium phase at around 1400°C in both V1 and V2. This had been noted previously in the calculations carried out during the alloy design process using a different program and data bank, MTDATA.

However, since gas evolution had never been reported in earlier 9Cr steels of this type, it was considered that the gas phase was, in practice, suppressed by kinetic factors and could be excluded from phase calculations for the sake of simplicity.

In the present calculations, the gas phase was included. Figure 1b shows phase stability curves for V2, the sample in which the porosity was the more severe. A domain of gas stability is present in the region between 1350 and 1500°C.

The same calculations were carried out for a number of other, successfully fabricated, VN-reinforced 9Cr steels. These showed that a domain of gas stability existed at equilibrium in those compositions with a relatively high nitrogen content (greater than ~ 0.05 wt.% N).

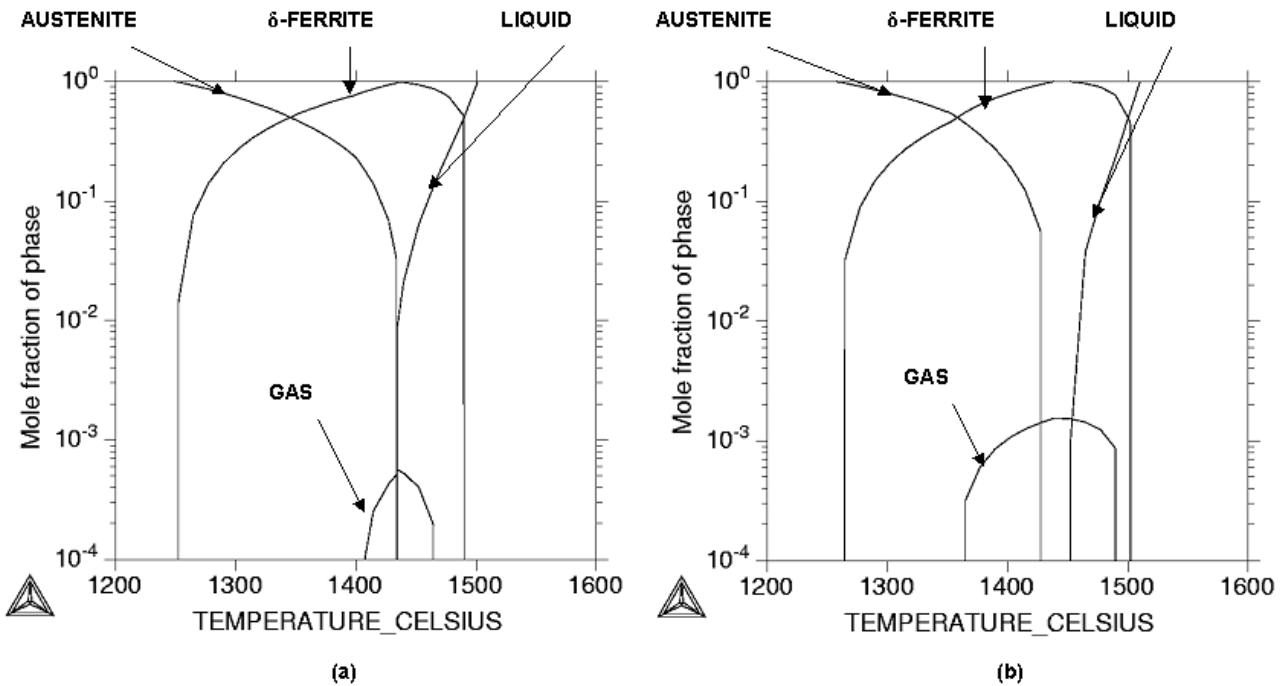


Figure 1 : Phase stability curves for (a) modified 9Cr1MoVNbN steel, (b) new VN-strengthened alloy V2

Examination of the stability regions of the liquid, δ -ferrite and austenite phases revealed that in V1, V2 and one other composition there was a temperature range in which δ -ferrite was the only stable major phase. For all the other compositions investigated, the liquid and austenite domains touched one another. An example is shown in figure 1a. Only the new alloys V1 and V2 display a region in which δ -ferrite and gas are the only stable phases.

The solubilities of carbon and nitrogen in ferrite are much lower than in austenite. A suggested mechanism of bubble formation is, therefore, that as solidification occurs, nitrogen is rejected from the δ -ferrite solidification front into the liquid. If austenite is present, the nitrogen can diffuse into it, but otherwise the liquid become supersaturated and allows the nucleation of bubbles.

It appears that the gas + δ -ferrite phase stability region is the origin of the porosity problem. Therefore, in order to avoid porosity, a composition must be chosen such that this region is eliminated (no region where the only solid phase is δ -ferrite).

EFFECTS OF COMPOSITION ON PHASE STABILITY IN NEW ALLOYS

In order to suggest new compositions, ThermoCalc was used to investigate the effect of each of the alloying elements on the temperature ranges of phase stability, and in particular the gas + δ -ferrite stability domain. The findings were as follows:

Mo and W: These are strong ferrite formers which increase the widths of both the gas stability domain and the gas + δ -ferrite region within this. Mo has a greater effect per unit mass.

Cr: This is also a ferrite stabiliser, but with a more complex effect than Mo and W. It diminishes the temperature range over which gas is stable but increases the gas + δ -ferrite region width. If our hypothesis on the origin of the porosity is correct, it would appear that Cr favours bubble formation.

Si and V: These elements modify the temperature at which the gas + δ -ferrite region occurs, but do not change its width. Si gives a slight increase in the width of the gas stability domain.

Mn and Ni: These decrease both the gas stability range and the gas + δ -ferrite region width, with Ni exerting a more pronounced effect than Mn for the same wt.% addition. Increasing the concentration of these elements would be favourable for the avoidance of porosity, but they appear to have a deleterious effect on creep properties, as reported in [1].

N: Figure 2 shows the effect of N on V2. As may be expected, an increase in the nitrogen content increases the range of temperatures over which the gas phase is stable. It is not present at all below a threshold level of just under 0.04 wt.%.

The width of the gas + δ -ferrite domain is not changed by further increases in the nitrogen content. However, at higher nitrogen concentrations, gas exists in equilibrium with liquid and with austenite (FCC).

C: The effect of C on V2 is shown in figure 3. A strong austenite former, it reduces the gas stability range and the width of the gas + δ -ferrite (high-temperature BCC) domain. At a critical carbon content of just over 0.1 wt.% C, this domain ceases to exist. This suggests that a relatively small increase in the carbon content of the new alloys could be sufficient to prevent porosity.

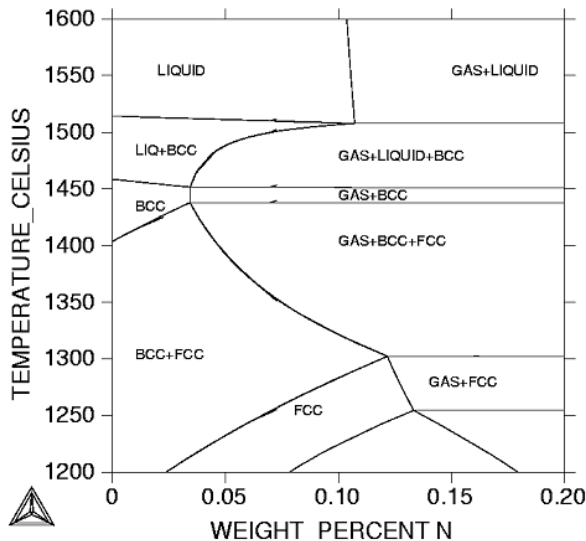


Figure 2 : Effect of nitrogen content on phase stability in the new VN-reinforced alloy V2

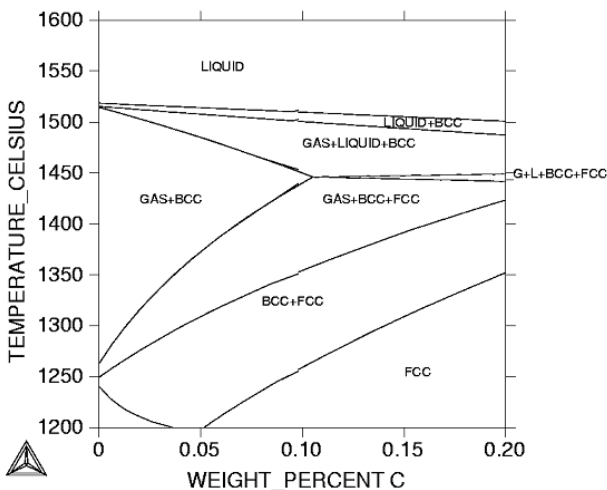


Figure 3 : Effect of carbon content on phase stability in the new VN-reinforced alloy V2

CONCLUSIONS AND FUTURE WORK

Small ingots of new reduced activation steels have been fabricated. The alloy based on reinforcement by TiC was produced successfully and can now be tested. However, the two alloys based on VN showed macroporosity. Thermodynamic calculations have been carried out to investigate the origin of this problem. From comparison between the new alloys and other, successfully fabricated materials of similar composition, it is believed that the porosity occurs if there is a temperature range for which gas and δ -ferrite are the only stable phases.

The effects of alloying elements on the extent of this gas + δ -ferrite domain have been investigated. Mn, Ni and C decrease the size of this region, while Cr, W and Mo increase it. It is believed that the most promising method of adapting the new alloys to avoid porosity problems is to increase the carbon content and, if necessary, slightly decrease the chromium and/or tungsten contents.

The next step for the VN-reinforced steels is to finalise a modified composition and submit an order for its fabrication.

REPORTS AND PUBLICATIONS

- [1] Y. DE CARLAN, "Conception de nouveaux alliages ferritiques-martensitiques à activation réduite optimisés pour la résistance au fluage". Final Report UT-TBM/MAT-LAM/DES, CEA report, NT SRMA 03-2526, February 2003.
- [2] Yardley, V. A., "Origin and avoidance of porosity in reduced-activation 9Cr steels optimised for creep strength", NT SRMA, to be printed.

TASK LEADER

Yann de CARLAN

DEN/DMN/SRMA
CEA-Saclay
F-91191 Gif-sur-Yvette Cedex

Tél. : 33 1 69 08 61 75
Fax : 33 1 69 08 71 30

E-mail : yann.decarlan@cea.fr

UT-TBM/MAT-Modpulse

Task Title: PULSED IRRADIATION OF THE MARTENSITIC ALLOY EUROFER
Preparation of samples for irradiations by krypton ions

INTRODUCTION

In the framework of the study of irradiation microstructure in ferritic stainless steel, the purpose is to investigate the secondary defects distribution to test the influence of the flux mode. Three modes are experimented at the same damage (3 dpa), two during the same time: cyclic (pulsed), continuous, and the third is a short time.

2003 ACTIVITIES

A. PREPARATION OF EUROFER SAMPLES FOR PULSED IRRADIATIONS

The material, delivered by SRMA (A. Alamo), is Eurofer97 [1] manufactured by Böhler (Austria) as plates in the normalized and tempered conditions, i.e.: normalized at 980°C (30 min) and tempered at 760°C (90 min). The chemical composition is given in table 1.

Table 1 : Chemical composition of Eurofer97

element	C	Cr	W	Ta	V
weight percent	0.12	8.96	1.04	0.15	0.18

element	Mn	Si	Ni	N	Nb
weight percent	0.48	0.03	0.06	0.022	<0.002

The material is a piece cut from a rolled plate (thickness: 25 mm). We defined three orientations: transverse (T), longitudinal (L), longitudinal-transverse (Lt).

The following mechanical slicing step consists to extract 500 µm thin plates by slicing with a saw in the three directions: L, T, Lt.

Then thinning is obtained down to a thickness of 100 µm in three steps: first, from each face, two 100 µm layers are removed successively with 400 and 600 mesh SiC paper.

The result is a foil of 100 µm thickness ready for the following step: electro-polishing. Disks for transmission electron microscope holders (diameter: 3 mm) are extracted from the foil by punching. Then, they are thinned in a double jet device (Tenupol 2 from STRUERS).

The prepared foils are observed and some pictures are recorded at low magnification (figure 1).

The microstructure is very similar from one foil to the other. It consists in laths containing a high density of dislocations. In some cases, it is possible to distinguish the initial grain boundaries between austenitic grains.

B. IRRADIATION CONDITIONS

The conditions are chosen to obtain a microstructure composed of loops with a density and a size that makes them easy to count.

The purpose is to compare various irradiation modes. A convenient damage corresponds to G = 3 displacements per atom, according to the bibliographic study.

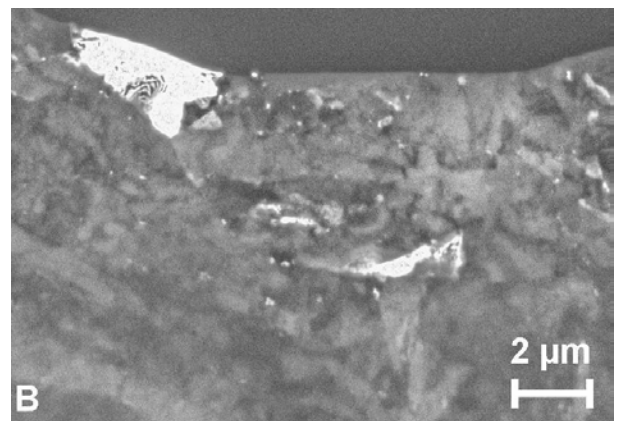
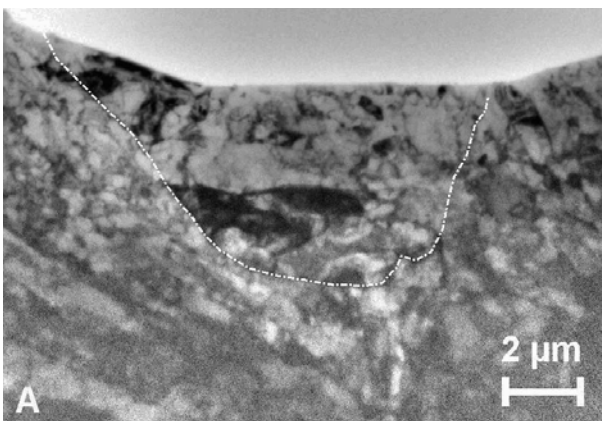


*Figure 1 : Low magnification image of Eurofer;
A: bright field with outlined gamma grain boundary, B: dark field lightening a lath*

The fluence required to obtain 3 dpa is deduced from the SRIM program (Stopping and Range of Ions in Matter) [2,3] using the Kinchin-Pease analytical solution. It gives the collision events per incident ion per angstrom (figure 2). From this curve, it appears that the maximum damage occurs at a depth p , equal to 100 nm from the surface and that the number of collision events at twice this maximum is close to the value at the entry. Moreover, this depth of 200 nm is the one suitable to observe small irradiation defects. This confirms that the energy of 700 keV is a right choice for irradiation of thin foils.

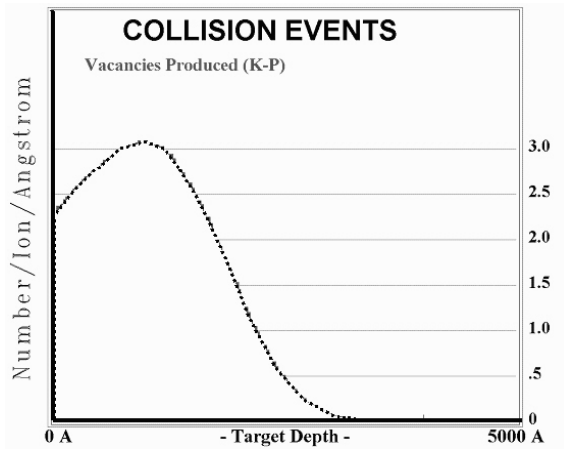


Figure 2 : Collision events versus depth penetration for a 700 keV, Kr ion in Fe/9%at.Cr from SRIM

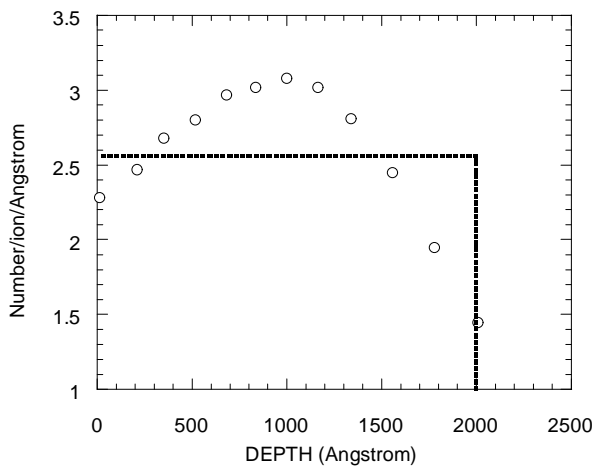


Figure 3 : Replot and chosen homogeneous distribution for 5186 collision events

Consequently, we calculate a mean value Δ_{mean} : 2.58 event/ion/angstrom, from integration from 0 to 2000 Å (figure 3):

$$\Delta_{mean} = \frac{\int_0^{2p} \Delta(x).dx}{2p}$$

The fluence is given by:

$$\Phi.t = \frac{G.n}{\Delta_{mean}}$$

with, irradiation duration t (seconds), ion flux Φ , atomic density n (for iron $n = 8.29.10^{22}$ atoms.cm⁻³), number of Frenkel pairs in a cascade P .

The overlapp between cascades is given from the cascade density H , such as $H.P = G.n$. This gives, the mean intercascade distance:

$$\rho = H^{-\frac{1}{3}}$$

with the wanted damage of 3 dpa, the irradiation parameters are given in table 2:

Table 2 : damage parameters

ion	energy	Damage G	Fluence $\Phi.t$	Intercascade distance, ρ
Kr ⁺⁺	700 keV	3 dpa	9.64.10 ¹⁴ ions.cm ⁻²	2,75 nm

The resulting flux necessary in the three irradiation modes is given in table 3.

In our study the cascade overlap is large as compared to individual cascades studies. These last, are conducted at low fluence.

They show that, as compared to fcc metals, the cascade efficiency (collapse ability) is reduced after irradiation by ions (low energy 80 keV Xe, < 5.10¹² cm⁻²) [4,5] and neutrons in reactor ($E > 1$ MeV, < 4.10¹⁹ n.cm⁻²) [6,7].

Table 3 : Irradiation conditions

pulsed irradiation, long time : 6 h pulse: 1 ms, cycle time: 20 ms		monotonous, long time : 6 h low flux		monotonous short time : 0.3 h high flux	
damage rate during pulse (dpa/s)	flux during pulse (ions/cm ² .s)	damage rate (dpa/s)	flux during pulse (ions/cm ² .s)	damage rate (dpa/s)	flux during pulse (ions/cm ² .s)
2.8.10 ⁻³	2.8.10 ⁻³	1.4 10 ⁻⁴	4.46.10 ¹⁰	2.8.10 ⁻³	8.9.10 ¹¹

CONCLUSIONS

The irradiations have been delayed. At time, available holders are ready for short time irradiations at 370 and 550°C.

The six irradiations will be performed at the end of march 2004. Three sets of samples for pulsed irradiations will be prepared in june 2004.

REFERENCES

- [1] Metallurgical characterization of as-received Eurofer97 products - C. A. Danon, S. Urvoy, A. Alamo - CEA report, NT SRMA 01-2418, March 2001.
- [2] Range algorithms - J. P. Biersack and L. Haggmark, - Nucl. Instr. and Meth., 174 (1980) 257.
- [3] The stopping and range of ions in Matter - vol. 2-6, Pergamon Press, 1977-1985.
- [4] Heavy-ion irradiation of alpha-iron - M. J. Jenkins, C. A. English and B. L. Eyre - Phil. Mag. 38, N°1 (1978) 97.
- [5] Xenon Ion irradiation of alpha-Fe - T. M. Robinson - Phys. Stat. Sol.(a) 75 (1983) 243.
- [6] Low dose neutron-irradiation damage in alpha-iron - I. M. Robertson, M. L. Jenkins, C. A. English - J. Nucl. Mater. 108 & 109 (1982) 209.
- [7] Low-dose neutron irradiation damage in fcc and bcc metals - C. A. English - J. Nucl. Mater. 108&109 (1982) 104.

REPORTS AND PUBLICATIONS

Preparation of Eurofer samples for pulsed irradiations - L. Boulanger and Y. Serruys, CEA report, NT DEN/SAC/DMN/SRMP 2004-01.

Microstructure of Eurofer and some martensitic steels Irradiated by neutrons, ions and electrons - L. Boulanger and Y.Serruys, CEA report, NT DEN/SAC/DMN/SRMP 2004-03, to be issued.

TASK LEADER

Loic BOULANGER

DEN/DMN/SRMP
CEA-Saclay
F-91191 Gif-sur-Yvette Cedex

Tél. : 33 1 69 08 64 19
Fax : 33 1 69 08 68 67

E-mail : loic.boulanger@cea.fr

Not available on line

Not available on line

Not available on line

Not available on line